Transcriptomic encoding of sensorimotor transformation in the midbrain

Zhiyong Xie[1,#], Mengdi Wang[2,3,#], Zeyuan Liu[2,3, #], Congping Shang[4,#], Changjiang Zhang[2,3], Le Sun[2,3,9], Huating Gu[1], Gengxin Ran[2,3], Qing Pei[1], Qiang Ma[2,3], Meizhu Huang[4], Junjing Zhang[5], Jiyao Zhang[5], Miao Zhao[1], Qian Wu[5, *], Peng Cao[1,8 *], Xiaoqun Wang[2,3,4,6,7,9,*]

[1] National Institute of Biological Sciences, Beijing 102206, China
[2] State Key Laboratory of Brain and Cognitive Science, CAS Center for Excellence in Brain Science and Intelligence Technology (Shanghai), Institute of Biophysics, Chinese Academy of Sciences, Beijing, 100101, China.
[3] University of Chinese Academy of Sciences, Beijing, 100049, China
[4] Bioland Laboratory (Guangzhou Regenerative Medicine and Health Guangdong Laboratory), Guangzhou, 510005, China
[5] State Key Laboratory of Cognitive Neuroscience and Learning, IDG/McGovern Institute for Brain Research, Beijing Normal University, Beijing, 100875, China
[6] Beijing Advanced Innovation Center for Big Data-Based Precision Medicine, Beihang University & Capital Medical University, Beijing, 100069, China
[7] Institute for Stem Cell and Regeneration, Chinese Academy of Sciences, Beijing, 100101, China
[8] Tsinghua Institute of Multidisciplinary Biomedical Research, Tsinghua University, Beijing 100084, China
[9] Beijing Institute for Brain Disorders, Capital Medical University, Beijing 100069, China

[#]These authors contributed equally
*Corresponding authors: xiaoqunwang@ibp.ac.cn (X.W.); caopeng@nibs.ac.cn (P.C.); qianwu@bnu.edu.cn (Q.W.)

ABSTRACT

Sensorimotor transformation, a process that converts sensory stimuli into motor actions, is critical for the brain to initiate behaviors. Although the circuitry involved in sensorimotor transformation has been well delineated, the molecular logic behind this process remains poorly understood. Here, we performed high-throughput and circuit-specific single-cell transcriptomic analyses of neurons in the superior colliculus (SC), a midbrain structure implicated in early sensorimotor transformation. We found that SC neurons in distinct laminae express discrete marker genes. Of particular interest, *Cbln2* and *Pitx2* are key markers that define glutamatergic projection neurons in the optic nerve (Op) and intermediate gray (InG) layers, respectively. The Cbln2+ neurons responded to visual stimuli mimicking cruising predators, while the Pitx2+ neurons encoded prey-derived vibrissal tactile cues. By forming distinct input and output connections with other brain areas, these neuronal subtypes independently mediate behaviors of predator avoidance and prey capture. Our results reveal that, in the midbrain, sensorimotor transformation for different behaviors may be performed by separate circuit modules that are molecularly defined by distinct transcriptomic codes.

INTRODUCTION

Sensorimotor transformation is a fundamental process in which the brain converts sensory information into motor command (Crochet et al., 2019; Franklin and Wolpert, 2011; Pouget and Snyder, 2000). The critical role of this process in sensory-guided behaviors has been demonstrated in diverse animal models, including fish (Bianco and Engert, 2015; Chen et al., 2018; Helmbrecht et al., 2018), rodents (Felsen and Mainen, 2008; Huda et al., 2020; Mayrhofer et al., 2019; Oliveira and Yonehara, 2018; Wang et al., 2020a), and primates (Buneo et al., 2002; Cavanaugh et al., 2012; Sparks, 1986). Although the brain circuits and computational models of sensorimotor transformation have been intensively studied, the molecular and genetic logic behind this process remains elusive.

Single-cell RNA sequencing (scRNA-seq) and single-nucleus RNA sequencing (snRNA-seq) are powerful approaches to identify the genes expressed in individual cells (Liu et al., 2020; Shapiro et al., 2013; Tang et al., 2009; Zhong et al., 2020; Zhong et al., 2018), enabling us to understand the cellular diversity and gene expression profiles of a specific brain region (Economo et al., 2018; Saunders et al., 2018; Zeisel et al., 2018). Moreover, by combining scRNA-seq with tools for circuit analysis, one should be able to link the transcriptomic heterogeneity to other characteristics of neurons such as their electrophysiological properties (Foldy et al., 2016), spatial distribution (Eng et al., 2019; Moffitt et al., 2018; Shah et al., 2016), neuronal activity (Hrvatin et al., 2018; Liu et al., 2020; Wu et al., 2017) and projection specificity (Tasic et al., 2018). Thus, scRNA-seq may provide an opportunity to explore the molecular and genetic logic of sensorimotor transformation.

In the mammalian brain, the superior colliculus (SC) is a midbrain structure for early sensorimotor transformation (Basso and May, 2017; Cang et al., 2018). The superficial layers of the SC, including the superficial grey layer (SuG) and the optic nerve layer (Op), are involved in visual information processing (De Franceschi and Solomon, 2018; Gale

and Murphy, 2014; Wang et al., 2010). The deep layers of the SC, including the intermediate layer and deep layer, participate in processing of tactile and auditory information (Cohen et al., 2008; Drager and Hubel, 1975). The deep layers of the SC control eye movement (Sparks, 1986; Wang et al., 2015), head movement (Isa and Sasaki, 2002; Wilson et al., 2018), and locomotion (Felsen and Mainen, 2008). From a neuroethological perspective, the sensorimotor transformations that occur in the SC enable it to orchestrate distinct behavioral actions in predator avoidance and prey capture (Dean et al., 1989; Oliveira and Yonehara, 2018). However，how different neuronal subtypes participate in these survival behaviors and the molecular features of these neurons remain unknown.

In the present study, by performing high-throughput and circuit-specific single-cell transcriptomic analyses of cells in the SC, we systematically studied the molecular markers of SC neurons, sensory response properties, input-output connectivity and their behavioral relevance. We found that Cbln2+ and Pitx2+ SC neurons form part of two distinct sets of circuit modules for sensorimotor transformation related to behaviors of predator avoidance and prey capture. Our data suggest that sensorimotor transformation for different behaviors may be performed by separate circuit modules that are molecularly defined by distinct transcriptomic codes.

RESULTS

A census of SC cell types using snRNA-seq

To understand the cell diversity of the SC, snRNA-seq of mouse SC was performed using the 10X Genomics Chromium Platform. From two experimental replicates, each containing six superior colliculi, 14,892 single-cell gene expression profiles were collected (Figures 1A, S1A, S1B; Table S1). In total, we found 9 major types of cells identified by the expression of classic marker genes; these were excitatory neurons, inhibitory neurons, astrocytes, oligodendrocyte progenitor cells (OPCs), oligodendrocytes, microglia, endothelial cells, ciliated cells and meningeal cells (Figures 1B, S1C). To further investigate neural diversity, we divided the excitatory and inhibitory neurons into 9 and 10 subclusters, respectively, each of which displayed a distinctive transcriptomic profile (Figure 1A, C, D; Table S2). The differentially expressed genes (DEGs) expressed by the cells in these subsets indicate that subclusters In-5 and In-10 are Calb1+ and Reln+ interneurons, respectively (Figure 1D).

Since the superior colliculus possesses a layered structure with a variety of circuit connections(ref), we next asked whether the subsets of neurons we identified are located in specific layers. To answer this question, we developed a method of spatial classification of mRNA expression data (SPACED) (https://github.com/xiaoqunwang-lab/SPACED; also see the methods section for details) through which we were able to assign a location score to each neural subset by analyzing RNA in situ hybridization images of the top DEGs in each subset from Allen Brain Atlas (https://mouse.brain-map.org) (Figures 1E, F, S1D). Using this method, a specificity score and the statistical significance were calculated for each subset, and it was found that the subsets of excitatory neurons and inhibitory neurons exhibited distinctive specificities for different layers of the SC (Figure 1E-G). Cells of subsets Ex-5/7/8/9 and In-2/7/8/10 were assigned to the superficial gray matter (SuG) layer, while cells in the Ex-3/6 and In-3 subsets highly expressed genes localized in the optic

nerve (Op) layer. In addition, Ex-1/4 and In-4 cells exhibited high spatial scores for the intermediate gray and white (InG/InWh) layers (Figures 1E-G and S1D) ($P < 0.05$). Although several neural subsets also showed relatively high spatial scores for certain layers, the data for those subsets did not meet the criteria for statistical significance, indicating that some neurons might be located in multiple layers. We next analyzed the Gene Ontology (GO) enrichment of the DEGs of cells that we assigned to different layers (Figure 1H). Intriguingly, the GO terms suggest that predicted SuG layer cells may play roles in visual learning and cognition, consistent with previous findings that cells in this layer receive signals from the retina and the visual cortex (Sparks, 1986). The GO analysis also indicated that cells that are predicted in the Op layer may be involved in defense and fear responses, while cells that are predicted in the InG layer may play roles in locomotor behavior (Figure 1H). These data suggest that neurons with diverse and distinctive transcriptomic profiles may be located in different layers of the SC.

Electrophysiological properties of LPTN- and ZI-projecting SC neurons

Several populations of glutamatergic neurons in the SC show distinctive projection patterns (Dean et al., 1989). To accurately visualize layer-specific neuronal projection patterns from the SC to downstream brain regions, we utilized a recently developed sparse-labeling strategy (Lin et al., 2018). We injected a mixture of AAV into the SC of vGlut2-IRES-Cre mice (Figure 2A) and performed morphological connectivity reconstruction by image tracing of individual cells (M-CRITIC) (https://github.com/xiaoqunwang-lab/M-CRITIC; also see the methods section for details). The complete morphological structure was reconstructed from multiple consecutive two-photon image-tracing stacks after alignment and was registered to the Allen Common Coordinate Framework (Figure 2B, Movie S1). One neuron with a cell body in the Op layer and dendritic ramifications in the SuG and Op layers extended its axon in the LPTN. Another neuron showed dendrites restricted to InG/InWh layer and a branched axon reaching the ZI (Figure 2C). To map how LPTN-projecting neurons are

distributed in the SC, we injected AAV2-retro-DIO-EGFP into the LPTN of vGlut2-IRES-Cre mice (Figure 2D). Retrogradely labeled EGFP+ SC neurons were predominantly localized within the Op layer (Figure 2E). With a similar strategy, we labeled ZI-projecting SC neurons with EGFP; these neurons are distributed in the InG/InWh and DpG layers of the SC (Figure 2F and 2G).

To compare the electrophysiological properties of these two neuronal populations, we performed whole-cell current-clamp recordings from LPTN-projecting and ZI-projecting SC neurons in acute SC slices (Figure S2A). These two populations of SC projection neurons did not show significant differences in resting membrane potential (Figure S2B) or firing threshold (Figure S2C). The number of action potentials fired by LPTN-projecting and ZI-projecting neurons in response to membrane depolarization also did not show a significant difference (Figure S2D and S2E). These data suggest that LPTN-projecting and ZI-projecting neurons are similar in their electrophysiological properties and that they cannot be distinguished using traditional electrophysiological measurements.

Projection-specific single-cell transcriptomic analysis

Next, we prepared acute SC slices and collected EGFP+ cells from the SC for patch-seq experiments (Cadwell et al., 2016b; Liu et al., 2020). In total, 78 cells were collected; 60 of these cells, including 21 LPTN-projecting neurons from the Op layer and 39 ZI-projecting neurons from the InG layer, passed the quality control test, with a median number of 7,746 gene expressed per cell (Figure S2F, S2G; Table S3). Examination of classic markers indicated that these cells were vGlut-expressing neurons and the neurons with different projections were clustered separately (Figure 2H), indicating that neurons with the same circuit connections may have similar innate gene expression profiles. We then further analyzed the DEGs of these two neuronal populations. The InG layer neurons projecting to ZI with soma in the SC highly expressed *Pitx2*, *Vwc2*, *Gsg1l*, *Clstn2*, and other genes, while LPTN-projecting Op layer

neurons highly expressed *Cbln2*, *Grm8*, *Zfp385b*, *Dgkh,* and other genes (Figure 2I, 2J, S2H, S2I；Table S4). On examination of the high-throughput snRNA-sequencing data, we found that 2 excitatory neuron subsets (Ex-3, 6) were assigned to the Op layer and 2 subsets (Ex-1, 4) belonged to the InG layer (Figure 1G). Transcriptomic correlation analysis indicated that Op-LPTN neurons and InG-ZI neurons identified through Patch-seq were similar to cells of the Ex-6 and Ex-4 subsets, respectively, in terms of their cellular gene expression profiles (Figure 2K). We next analyzed the DEGs of two subsets of cells from the Op layer (Ex-3 vs. Ex6) and the InG layer (Ex-1 vs. Ex-4) (Figure 2L, 2M; Table S5). We found that some projection-specific genes were restricted to one subset of cells (Figures 2L-N, S2J). For example, as a marker gene of Op-LPTN projection neurons, *Cbln2* was expressed in both Ex-3 and Ex-6 cells, while *Dgkh* was only highly expressed in Ex-6 cells (Figure 2L, 2N). Among genes that were specifically expressed in InG-ZI projection neurons, *Pitx2* was exclusively expressed in Ex-4 neurons, but *Vwc2* was expressed in both subsets of neurons (Figure 2M, 2N). These data suggest that the projection-specific SC neurons represent subpopulations of neurons in specific SC layers that can be distinguished by their gene expression profiles.

Roles of Cbln2+ and Pitx2+ SC neurons in sensory-triggered behaviors related to predator avoidance and prey capture

Cbln2 and *Pitx2* were highly expressed in LPTN-projecting and ZI-projecting SC neurons, respectively (Figure 2I)**,** which also displayed the highest fidelity of Op and InG layer specificity based on our analysis of in situ RNA hybridization images from Allen Brain Atlas (https://mouse.brain-map.org) (Figure S3A). To examine whether *Cbln2* acts as a key molecular marker of SC circuits associated with predator avoidance, we generated Cbln2-IRES-Cre mouse line (Figure S3B, S3C). We first tested whether it is possible to specifically label Cbln2+ SC neurons in Cbln2-IRES-Cre mice by injecting AAV-DIO-EGFP into the SC of these mice. EGFP-expressing neurons were distributed predominantly in the Op layer of the SC (Figure 3A). More than 90% of

EGFP-expressing SC neurons were positive for *Cbln2* mRNA (91% ± 9%, n=3 mice), and SC neurons expressing *Cbln2* mRNA were predominantly positive for EGFP (92% ± 11%, n=3 mice), suggesting that it is possible to specifically label Cbln2+ neurons in the SC of Cbln2-IRES-Cre mice (Figure 3B). In addition, EGFP-expressing SC neurons were mostly positive for *vGlut2* mRNA (93% ± 6%, n=3 mice), and very few were positive for *vGAT* mRNA (4% ± 2.1%, n=3 mice), confirming that the Cbln2+ SC neurons were predominantly glutamatergic (Figure S3D).

Under laboratory conditions, mice exhibit a freezing response to an overhead moving visual target; this is an innate behavior that may be crucial to the avoidance of aerial predators in the natural environment (De Franceschi et al., 2016). We assessed the role of Cbln2+ SC neurons in this behavior (Figure 3C) by selectively silencing Cbln2+ SC neurons using tetanus neurotoxin (TeNT) (Schiavo et al., 1992). AAV-DIO-EGFP-2A-TeNT was bilaterally injected into the SC of Cbln2-IRES-Cre mice, resulting in the expression of EGFP and TeNT in Cbln2+ SC neurons (Figure S3E). The effectiveness and specificity of TeNT-mediated synaptic inactivation of SC neurons have been validated in earlier studies (Shang et al., 2018; Shang et al., 2019). We found that control mice with Cbln2+ SC neurons expressing EGFP (Ctrl) exhibited freezing in response to an overhead moving visual target (Movie S2; black trace in Figure 3D). In contrast, synaptic inactivation of Cbln2+ SC neurons by TeNT strongly impaired visually evoked freezing responses (Movie S2; red trace in Figure 3D). Quantitative analyses indicated that synaptic inactivation of Cbln2+ SC neurons caused a significant increase in locomotion speed during visual stimuli but not before or after visual stimuli (Figure 3, E-G). However, inactivation of Cbln2+ SC neurons did not alter the efficiency of predatory hunting (Figure S3, F-I). These data suggest that Cbln2+ SC neurons are selectively required for a visually evoked freezing response in mice.

To examine whether *Pitx2* acts as a key molecular marker of SC circuits for prey capture, we studied the Pitx2-Cre knock-in line (Liu et al., 2003). We first examined

whether it is possible to specifically label Pitx2+ SC neurons in Pitx2-Cre mice by injecting AAV-DIO-EGFP into the SC of these mice. EGFP-expressing neurons were distributed predominantly in the intermediate layers of the SC (Figure 3H). Most EGFP-expressing SC neurons were positive for *Pitx2* mRNA (88% ± 8%, n=3 mice), and SC neurons expressing *Pitx2* mRNA were predominantly positive for EGFP (89% ± 9%, n=3 mice), suggesting that Pitx2+ SC neurons were specifically labeled in Pitx2-Cre mice (Figure 3I). Moreover, most EGFP-expressing SC neurons were positive for *vGlut2* mRNA (95% ± 7%, n=3 mice), and very few were positive for *vGAT* mRNA (6% ± 2.5%, n=3 mice), confirming that Pitx2+ SC neurons are predominantly glutamatergic (Figure S3J).

To explore the role of Pitx2+ SC neurons in prey capture (Figure 3J), we injected AAV-DIO-EGFP-2A-TeNT into the SC of Pitx2-Cre mice; this resulted in the expression of EGFP and TeNT in Pitx2+ SC neurons (Figure S3K). Synaptic inactivation of Pitx2+ SC neurons impaired prey capture (Movie S3; Figure 3K) by increasing the latency to attack (Figure 3L), prolonging the time required for prey capture (Figure 3M), and reducing the frequency of attack (Figure 3N). However, the visually evoked freezing response was not impaired in these mice, as evidenced by a lack of significant changes in locomotion speed before, during or after the presentation of visual stimuli (Figure S3, L-O). These data suggest that Pitx2+ SC neurons are selectively required for prey capture behavior in mice.

Cbln2+ and Pitx2+ SC neurons encode distinct sensory stimuli

Next, we addressed how Cbln2+ and Pitx2+ SC neurons participate in predator avoidance and prey capture. Rodents use vision to detect aerial predators (De Franceschi et al., 2016; Yilmaz and Meister, 2013), whereas they use vibrissal tactile information (Anjum et al., 2006) and vision (Hoy et al., 2016) for prey capture. To examine whether Cbln2+ and Pitx2+ SC neurons process visual and vibrissal tactile information, we expressed GCaMP7 in these neurons and implanted an optical fiber

above the neurons (Figure 4, A and B) (Dana et al., 2019; Gunaydin et al., 2014). We provided visual and vibrissal tactile stimuli to head-fixed mice standing on a treadmill and simultaneously performed fiber photometry to record GCaMP fluorescence in these neurons (Figure 4C). The visual stimulus was a computer-generated black circle (5° or 25° in diameter) moving at a controlled velocity (32°/s or 128°/s) across the visual receptive field (RF) on a tangent screen (Shang et al., 2019). The vibrissal tactile stimuli, which were designed to mimic the tactile cues produced by moving prey, were brief gentle air puffs (100 ms, 0~40 p.s.i.) directed toward the vibrissal region contralateral or ipsilateral to the recorded side (Shang et al., 2019).

We found that the centers of the visual receptive fields of Cbln2+ SC neurons were distributed predominantly in the dorsal quadrants of the visual field (Figure S4A). These neurons responded broadly to visual stimuli moving in various directions, with a preference for the temporal-to-nasal direction (Figure 4, D and H). In addition, they responded more strongly to circles moving at lower velocity (Figure 4, E and I) and those with smaller diameters (Figure 4, F and J). However, the Cbln2+ SC neurons did not respond to air puffs applied to the vibrissal area (Figure S4B). Unlike Cbln2+ SC neurons, Pitx2+ SC neurons responded to air puffs directed toward the vibrissal region contralateral to the recorded side (Figure 4, G and K). However, they did not respond to moving visual stimuli (Figure S4, C-E). These data indicate that Cbln2+ SC neurons may specifically process visual information derived from an aerial cruising predator, while Pitx2+ SC neurons may be selectively involved in processing vibrissal tactile stimuli mimicking moving prey. Thus, Cbln2+ and Pitx2+ SC neurons may comprise two distinct sets of circuit modules that are used to detect visual cues produced by aerial predator and vibrissal cues produced by terrestrial prey of mice.

Cbln2+ and Pitx2+ SC neurons receive distinct monosynaptic inputs

Next, we performed monosynaptic retrograde tracing using recombinant rabies virus (RV) (Wickersham et al., 2007) to examine how Cbln2+ and Pitx2+ SC neurons are

connected with neural structures associated with sensory information processing (Figure 5, A-C; Figure S5, A and B). A brain-wide survey revealed a number of monosynaptic projections to Cbln2+ and Pitx2+ SC neurons (Figure 5, D-G; Figure S5, C-F). First, Cbln2+ SC neurons are monosynaptically innervated by a subset of retinal ganglion cells in the contralateral retina (Figure 5D) and neurons in layer 5 of the ipsilateral primary visual cortex (V1) (Figure 5E). In contrast, Pitx2+ SC neurons did not receive monosynaptic inputs from these visual structures (Figure 5D and 5E). Second, Pitx2+ SC neurons, but not Cbln2+ SC neurons, receive robust monosynaptic inputs from the subnuclei of the trigeminal complex (Pr5 and Sp5) (Figure 5F; Figure S5C), the primary somatosensory cortex (S1) (Figure 5G), and the ZI (Figure S5D), which are involved in processing tactile information. Third, Pitx2+ SC neurons, but not Cbln2+ SC neurons, also receive monosynaptic inputs from motor-related brain areas (e.g., SNr and M1/M2) (Figure S5, E and F) and the cingulate cortex (Cg1/2) (Figure S5F). Quantitative analysis of retrogradely labeled cells in various brain areas indicated that Cbln2+ and Pitx2+ SC neurons may receive two sets of presynaptic inputs that are mutually exclusive (Figure 5H). These morphological data support the hypothesis that Cbln2+ and Pitx2+ SC neurons belong to two distinct sets of circuit modules that are used to detect visual cues produced by aerial predators (retina and V1) and tactile cues produced by terrestrial prey (Pr5, Sp5, S1 and ZI) of mice.

Target-specific projections of Cbln2+ and Pitx2+ SC neurons

To map the efferent projections of Cbln2+ and Pitx2+ SC neurons, we injected AAV-DIO-EGFP into Cbln2-IRES-Cre and Pitx2-IRES-Cre mice, resulting in the expression of EGFP in Cbln2+ and Pitx2+ neurons in the SC (Figure 6, A and B). In the LPTN, we found strong EGFP+ axonal projections from Cbln2+ SC neurons but not from Pitx2+ SC neurons (Figure 6C). Quantitative analyses of EGFP fluorescence indicated that the density of EGFP+ axons from Cbln2+ SC neurons was significantly higher than that from Pitx2+ SC neurons in the LPTN (Figure 6D). These data suggest that Cbln2+

SC neurons, but not Pitx2+ SC neurons, send strong projections to the LPTN. Similarly, in the ZI, we found strong EGFP+ axonal projections from Pitx2+ SC neurons but not from Cbln2+ SC neurons (Figure 6E). Quantitative analysis of the EGFP fluorescence indicated that, in the ZI, the density of EGFP+ axons from Pitx2+ SC neurons was significantly higher than that of EGFP+ axons from Cbln2+ SC neurons (Figure 6F). These data suggest that Pitx2+ SC neurons, but not Cbln2+ SC neurons, send strong projections to the ZI.

We also explored the target-specific projections of Cbln2+ and Pitx2+ SC neurons using retrograde AAV (Tervo et al., 2016). AAV2-retro-DIO-EGFP was injected into the LPTN of Cbln2-IRES-Cre mice, followed by injection of AAV-DIO-mCherry into the SC (Figure 6G). More than 80% of mCherry+ SC neurons (83% ± 9%, n=3 mice) were labeled by EGFP, suggesting that a large proportion of Cbln2+ SC neurons project to the LPTN (Figure 6, H and I). We injected AAV2-retro-DIO-EGFP into the ZI of Pitx2-Cre mice, followed by injection of AAV-DIO-mCherry into the SC (Figure 6J). More than two-thirds of mCherry+ SC neurons (72% ± 11%, n=3 mice) were labeled by EGFP, suggesting that a large proportion of Pitx2+ neurons project to the ZI (Figure 6, K and L).

We also compared the brain-wide projections of Cbln2+ and Pitx2+ SC neurons (Figure S6A). In addition to the LPTN and the ZI, Cbln2+ and Pitx2+ SC neurons also sent descending projections to a number of areas in the midbrain, pons and medulla. Strikingly, their divergent projection targets rarely overlap (Figure S6, B-F), supporting the hypothesis that these two subtypes of SC neurons are functionally distinct.

Activation of the Cbln2+ SC-LPTN pathway and the Pitx2+ SC-ZI pathway

The above data indicate that Cbln2+ and Pitx2+ neurons in the SC selectively project to the LPTN and to the ZI, respectively. To test the behavioral relevance of the Cbln2+ SC-LPTN pathway, we injected AAV-DIO-ChR2-mCherry into the SC of Cbln2-IRES-Cre mice (Boyden et al., 2005), followed by implantation of an optical fiber above the LPTN (Figure 7A). In acute SC slices, light stimulation (10 Hz or 20 Hz, 2 ms,

10 pulses) effectively evoked action potential firing by neurons expressing ChR2-mCherry (Figure S7, A and B). We found that light stimulation of ChR2-mCherry+ axon terminals of Cbln2+ SC neurons in the LPTN induced a freezing response in mice (Movie S4; Figure 7, B and C), as evidenced by a selective reduction of locomotion speed during light stimulation (Figure 7D). However, activation of this pathway did not alter the efficiency of prey capture during predatory hunting (Figure S7, D and E). These data indicate that activation of the Cbln2+ SC-LPTN pathway selectively triggers predator avoidance rather than prey capture.

Next, we examined the behavioral relevance of the Pitx2+ SC-ZI pathway. AAV-DIO-ChR2-mCherry was injected into the SC of Pitx2-Cre mice, followed by implantation of an optical fiber above the ZI (Figure 7E). In acute SC slices, light stimulation (10 Hz or 20 Hz, 2 ms, 10 pulses) evoked phase-locked action potential firing by neurons expressing ChR2-mCherry (Figure S7C). Photostimulation of ChR2-mCherry+ axon terminals of Pitx2+ SC neurons in the ZI did not evoke a freezing response (Figure S7, F and G). However, activation of this pathway promoted predatory hunting (Movie S5; Figure 7, F and G) by decreasing the latency to hunt (Figure 7H), reducing the time required for prey capture (Figure 7I), and increasing the frequency of predatory attacks (Figure 7J). These data indicate that activation of the Pitx2+ SC-ZI pathway selectively promotes prey capture without inducing predator avoidance.

DISCUSSION

The SC of the midbrain is a classical model for the study of early sensorimotor transformation related to sensory-triggered innate behaviors (fish (Bianco and Engert, 2015); rodents (Dean et al., 1989); primates (Sparks, 1986)). In mice, a series of projection-defined SC circuits have been linked to sensory-triggered innate behaviors such as predator avoidance (Evans et al., 2018; Shang et al., 2018; Shang et al., 2015; Wei et al., 2015; Zhou et al., 2019) and prey capture (Hoy et al., 2019; Shang et al., 2019). However, the number of cell types in the SC, their molecular signatures, their projection patterns, and their functional roles in these behaviors remain unclear. Here, we used a combined approach consisting of single-cell transcriptomic analysis and circuit analysis to address the above questions.

Using high-throughput single-cell transcriptomic analyses, we first systematically analyzed the cell-type diversity of the SC. We found that the majority of neuronal subtypes defined by gene expression patterns showed layer-specific distribution in the SC (Figure 1). To better understand the correlation between projection patterns and transcriptomics, we performed projection-specific scRNA-Seq of cells in the SC-LPTN and SC-ZI pathways and identified Cbln2 and Pitx2 as key molecular markers for SC neurons with different projections (Figure 2). Cbln2+ and Pitx2+ SC neurons, distributed in distinct layers of the SC, are functionally involved in predator avoidance and prey capture behavior, respectively (Figure 3). Strikingly, these two neuronal subtypes process neuroethological information received through distinct sensory modalities (Figure 4) and are connected to almost completely different sets of input-output synaptic connectomes (Figures 5 and 6). Finally, activation of the Cbln2+ SC-LPTN and the Pitx2+ SC-ZI pathways copied the behavioral phenotypes of SC-LPTN and SC-ZI pathways (Figure 7).

We believe our data allow two conclusions. First, they reveal that it is the

transcriptomically-defined neuronal subtypes and their projections, when combined together, define early sensorimotor transformation and the subsequent behavior (Figure 7K and 7L). This finding supports the hypothesis that transcriptomically-defined circuit modules correspond to specific behaviors. Previous studies of this "correspondence" question in the hypothalamus and prefrontal cortex, two brain areas that are involved in the regulation of motivation and cognition, did not find a clear correspondence between transcriptomically defined neurons and behaviors (Kim et al., 2019; Lui et al., 2021; Moffitt et al., 2018). In combination with these pioneering studies, our results suggest that the circuit design of sensorimotor transformation in the midbrain, which requires precise detection of sensory features and rapid initiation of innate behaviors, may differ from the circuit design in brain areas that are responsible for complex information processing such as that related to the regulation of motivation and cognition.

Second, our data identified Cbln2 and Pitx2 as discrete markers that label neurons in the Op and InG layers of the SC. Intriguingly, we found three Op subtypes (2 subtypes of excitatory neurons; 1 subtype of inhibitory neurons) and three InG/InWh subtypes (2 subtypes of excitatory neurons; 1 subtype of inhibitory neurons) in our unsupervised high-throughput single-cell transcriptome and spatial information analyses. Cbln2 was extensively expressed by two subtypes of Op layer excitatory neurons, but Pitx2 was expressed by only one subtype of InG layer excitatory neurons, indicating the heterogeneity of neurons located in different SC layers. Our data also suggest that neurons with similar transcriptomic profiles may tend to participate in the same projection paths and to play a role in the regulation of behavior.

Cbln2 and other members of the Cerebellin family are synaptic organizer molecules that bind to presynaptic neurexins and to postsynaptic receptors (Cheng et al., 2016). Recent studies have shown that Cbln2 may participate in synapse formation (Matsuda and Yuzaki, 2011; Seigneur and Sudhof, 2018). It remains to be determined whether

Cbln2 in Cbln2-expressing SC neurons participates in the formation of the SC-LPTN pathway. As a transcription factor, Pitx2 participates in the migration of collicular neurons during brain development (Waite et al., 2013). In the adult brain, activation of Pitx2+ SC neurons elicited stereotyped head displacements in a body-referenced frame (Masullo et al., 2019). However, the functional role of Pitx2+ SC neurons in naturalistic behavioral context has not been demonstrated in this study. Our study has shown that Pitx2+ SC neurons specifically participate in predatory hunting, a goal-directed behavior that occurs in natural environment.

Our results also raise new questions. First, it is unclear how the genes expressed by Cbln2+ and Pitx2+ SC neurons participate in the formation and function of the Cbln2+ SC-LPTN and Pitx2+ SC-ZI pathways. Single-cell transcriptomic analyses of Cbln2+ and Pitx2+ SC neurons at different developmental stages and genetic manipulations of these neurons may be performed to address this question. Second, the neural substrate that mediates the interactions between the two distinct circuit modules for predator avoidance and prey capture remains to be studied. With the identification of Cbln2+ and Pitx2+ SC neurons, their distinct input-output synaptic connectomes, and the demonstration of their roles in sensory-triggered innate behaviors in hand, these questions can now be addressed.

AUTHOR CONTRIBUTIONS

X.W., P.C. and Q. W. conceived the study, designed the experiments and wrote the manuscript. Z. L., Q. M. and J. Z. performed the snRNA-seq experiment. C. Z., L. S. and G. R. carried out the Patch-seq experiment. M. W. and Q. W. analyzed the RNA-seq data. Z. L., C.Z and L. S. did the neuron projection 3D reconstruction. J. Z. prepared the animal samples. Z.X., C.S., and M.H. performed viral injections and optical fiber implantations. Z.X. did fiber photometry recording and data analyses. Z.X. did rabies virus tracing and data analyses. H.G. and C.S. did behavioral tests and data analyses. Q.P. and Z.X. did immunohistochemistry and data analyses. H.G. did slice physiology. All authors edited and proofed the manuscript.

ACKNOWLEDGMENTS

We thank Karl Deisseroth for providing plasmids. We also thank the members of the Neuroscience Pioneer Club for valuable discussions. This work was supported by the National Key R&D Program of China (2019YFA0110100), the National Basic Research Program of China (2017YFA0102601, 2017YFA0103303), the Strategic Priority Research Program of the Chinese Academy of Sciences (XDA16020601, XDB32010100), the National Natural Science Foundation of China (NSFC) (31925019 to P.C. and 31771140, 81891001 to X. W.) , the BUAA-CCMU Big Data and Precision Medicine Advanced Innovation Center Project (BHME-2019001) to X. W, and the institutional grants from the Chinese Ministry of Science and Technology to NIBS.

COMPETING FINANCIAL INTERESTS

The authors declare no competing financial interests.

REFERENCES

Anjum, F., Turni, H., Mulder, P.G., van der Burg, J., and Brecht, M. (2006). Tactile guidance of prey capture in Etruscan shrews. Proceedings of the National Academy of Sciences of the United States of America *103*, 16544-16549.

Basso, M.A., and May, P.J. (2017). Circuits for Action and Cognition: A View from the Superior Colliculus. Annu Rev Vis Sci *3*, 197-226.

Bianco, I.H., and Engert, F. (2015). Visuomotor transformations underlying hunting behavior in zebrafish. Current biology : CB *25*, 831-846.

Boyden, E.S., Zhang, F., Bamberg, E., Nagel, G., and Deisseroth, K. (2005). Millisecond-timescale, genetically targeted optical control of neural activity. Nature neuroscience *8*, 1263-1268.

Buneo, C.A., Jarvis, M.R., Batista, A.P., and Andersen, R.A. (2002). Direct visuomotor transformations for reaching. Nature *416*, 632-636.

Butler, A., Hoffman, P., Smibert, P., Papalexi, E., and Satija, R. (2018). Integrating single-cell transcriptomic data across different conditions, technologies, and species. Nature biotechnology *36*, 411-420.

Cadwell, C.R., Palasantza, A., Jiang, X., Berens, P., Deng, Q., Yilmaz, M., Reimer, J., Shen, S., Bethge, M., and Tolias, K.F. (2016a). Electrophysiological, transcriptomic and morphologic profiling of single neurons using Patch-seq. Nature biotechnology *34*, 199-203.

Cadwell, C.R., Palasantza, A., Jiang, X., Berens, P., Deng, Q., Yilmaz, M., Reimer, J., Shen, S., Bethge, M., Tolias, K.F., *et al.* (2016b). Electrophysiological, transcriptomic and morphologic profiling of single neurons using Patch-seq. Nature biotechnology *34*, 199-203.

Cang, J., Savier, E., Barchini, J., and Liu, X. (2018). Visual Function, Organization, and Development of the Mouse Superior Colliculus. Annu Rev Vis Sci *4*, 239-262.

Cavanaugh, J., Monosov, I.E., McAlonan, K., Berman, R., Smith, M.K., Cao, V., Wang, K.H., Boyden, E.S., and Wurtz, R.H. (2012). Optogenetic inactivation modifies monkey visuomotor behavior. Neuron *76*, 901-907.

Chen, J., Cheng, M., Wang, L., Zhang, L., Xu, D., Cao, P., Wang, F., Herzog, H., Song, S., and Zhan, C. (2020). A Vagal-NTS Neural Pathway that Stimulates Feeding. Current biology : CB *30*, 3986-3998 e3985.

Chen, S., Huang, T., Zhou, Y., Han, Y., Xu, M., and Gu, J. (2017). AfterQC: automatic filtering, trimming, error removing and quality control for fastq data. BMC bioinformatics *18*, 91-100.

Chen, X., Mu, Y., Hu, Y., Kuan, A.T., Nikitchenko, M., Randlett, O., Chen, A.B., Gavornik, J.P., Sompolinsky, H., Engert, F., *et al.* (2018). Brain-wide Organization of Neuronal Activity and Convergent Sensorimotor Transformations in Larval Zebrafish. Neuron *100*, 876-890 e875.

Cheng, S., Seven, A.B., Wang, J., Skiniotis, G., and Ozkan, E. (2016). Conformational Plasticity in the Transsynaptic Neurexin-Cerebellin-Glutamate Receptor Adhesion Complex. Structure *24*, 2163-2173.

Cohen, J.D., Hirata, A., and Castro-Alamancos, M.A. (2008). Vibrissa sensation in superior colliculus: wide-field sensitivity and state-dependent cortical feedback. The Journal of neuroscience : the official journal of the Society for Neuroscience *28*, 11205-11220.

Crochet, S., Lee, S.H., and Petersen, C.C.H. (2019). Neural Circuits for Goal-Directed Sensorimotor Transformations. Trends in neurosciences *42*, 66-77.

Cusanovich, D.A., Hill, A.J., Aghamirzaie, D., Daza, R.M., Pliner, H.A., Berletch, J.B., Filippova, G.N., Huang, X., Christiansen, L., and DeWitt, W.S. (2018). A single-cell atlas of in vivo mammalian chromatin accessibility. Cell *174*, 1309-1324. e1318.

Dana, H., Sun, Y., Mohar, B., Hulse, B.K., Kerlin, A.M., Hasseman, J.P., Tsegaye, G., Tsang, A., Wong, A., Patel, R., *et al.* (2019). High-performance calcium sensors for imaging activity in neuronal populations and microcompartments. Nature methods *16*, 649-657.

De Franceschi, G., and Solomon, S.G. (2018). Visual response properties of neurons in the superficial layers of the superior colliculus of awake mouse. J Physiol *596*, 6307-6332.

De Franceschi, G., Vivattanasarn, T., Saleem, A.B., and Solomon, S.G. (2016). Vision Guides Selection of Freeze or Flight Defense Strategies in Mice. Current biology : CB *26*, 2150-2154.

Dean, P., Redgrave, P., and Westby, G.W. (1989). Event or emergency? Two response systems in the mammalian superior colliculus. Trends in neurosciences *12*, 137-147.

Dobin, A., Davis, C.A., Schlesinger, F., Drenkow, J., Zaleski, C., Jha, S., Batut, P., Chaisson, M., and Gingeras, T.R. (2013). STAR: ultrafast universal RNA-seq aligner. Bioinformatics *29*, 15-21.

Drager, U.C., and Hubel, D.H. (1975). Responses to visual stimulation and relationship between visual, auditory, and somatosensory inputs in mouse superior colliculus. Journal of neurophysiology *38*, 690-713.

Economo, M.N., Viswanathan, S., Tasic, B., Bas, E., Winnubst, J., Menon, V., Graybuck, L.T., Nguyen, T.N., Smith, K.A., Yao, Z., *et al.* (2018). Distinct descending motor cortex pathways and their roles in movement. Nature *563*, 79-84.

Eng, C.L., Lawson, M., Zhu, Q., Dries, R., Koulena, N., Takei, Y., Yun, J., Cronin, C., Karp, C., Yuan, G.C., *et al.* (2019). Transcriptome-scale super-resolved imaging in tissues by RNA seqFISH. Nature *568*, 235-239.

Evans, D.A., Stempel, A.V., Vale, R., Ruehle, S., Lefler, Y., and Branco, T. (2018). A synaptic threshold mechanism for computing escape decisions. Nature *558*, 590-594.

Felsen, G., and Mainen, Z.F. (2008). Neural substrates of sensory-guided locomotor decisions in the rat superior colliculus. Neuron *60*, 137-148.

Foldy, C., Darmanis, S., Aoto, J., Malenka, R.C., Quake, S.R., and Sudhof, T.C. (2016). Single-cell RNAseq reveals cell adhesion molecule profiles in electrophysiologically defined neurons. Proceedings of the National Academy of Sciences of the United States of America *113*, E5222-5231.

Franklin, D.W., and Wolpert, D.M. (2011). Computational mechanisms of sensorimotor control. Neuron *72*, 425-442.

Gale, S.D., and Murphy, G.J. (2014). Distinct representation and distribution of visual information by specific cell types in mouse superficial superior colliculus. The Journal of neuroscience : the official journal of the Society for Neuroscience *34*, 13458-13471.

Gunaydin, L.A., Grosenick, L., Finkelstein, J.C., Kauvar, I.V., Fenno, L.E., Adhikari, A., Lammel, S., Mirzabekov, J.J., Airan, R.D., Zalocusky, K.A., *et al.* (2014). Natural neural projection dynamics underlying social behavior. Cell *157*, 1535-1551.

Haghverdi, L., Lun, A.T., Morgan, M.D., and Marioni, J.C. (2018). Batch effects in single-cell RNA-sequencing data are corrected by matching mutual nearest neighbors. Nature biotechnology *36*, 421-427.

Helmbrecht, T.O., Dal Maschio, M., Donovan, J.C., Koutsouli, S., and Baier, H. (2018). Topography of a Visuomotor Transformation. Neuron *100*, 1429-1445 e1424.

Hoy, J.L., Bishop, H.I., and Niell, C.M. (2019). Defined Cell Types in Superior Colliculus Make Distinct Contributions to Prey Capture Behavior in the Mouse. Current biology : CB *29*, 4130-4138 e4135.

Hoy, J.L., Yavorska, I., Wehr, M., and Niell, C.M. (2016). Vision Drives Accurate Approach Behavior during Prey Capture in Laboratory Mice. Current biology : CB *26*, 3046-3052.

Hrvatin, S., Hochbaum, D.R., Nagy, M.A., Cicconet, M., Robertson, K., Cheadle, L., Zilionis, R., Ratner, A., Borges-Monroy, R., Klein, A.M.*, et al.* (2018). Single-cell analysis of experience-dependent transcriptomic states in the mouse visual cortex. Nature neuroscience *21*, 120-129.

Huda, R., Sipe, G.O., Breton-Provencher, V., Cruz, K.G., Pho, G.N., Adam, E., Gunter, L.M., Sullins, A., Wickersham, I.R., and Sur, M. (2020). Distinct prefrontal top-down circuits differentially modulate sensorimotor behavior. Nature communications *11*, 6007.

Isa, T., and Sasaki, S. (2002). Brainstem control of head movements during orienting; organization of the premotor circuits. Progress in neurobiology *66*, 205-241.

Kim, D.W., Yao, Z., Graybuck, L.T., Kim, T.K., Nguyen, T.N., Smith, K.A., Fong, O., Yi, L., Koulena, N., Pierson, N.*, et al.* (2019). Multimodal Analysis of Cell Types in a Hypothalamic Node Controlling Social Behavior. Cell *179*, 713-728 e717.

Liao, Y., Smyth, G.K., and Shi, W. (2014). featureCounts: an efficient general purpose program for assigning sequence reads to genomic features. Bioinformatics *30*, 923-930.

Lin, R., Wang, R., Yuan, J., Feng, Q., Zhou, Y., Zeng, S., Ren, M., Jiang, S., Ni, H., Zhou, C.*, et al.* (2018). Cell-type-specific and projection-specific brain-wide reconstruction of single neurons. Nature methods *15*, 1033-1036.

Liu, J., Wang, M., Sun, L., Pan, N.C., Zhang, C., Zhang, J., Zuo, Z., He, S., Wu, Q., and Wang, X. (2020). Integrative analysis of in vivo recording with single-cell RNA-seq data reveals molecular properties of light-sensitive neurons in mouse V1. Protein & cell *11*, 417-432.

Liu, W., Selever, J., Lu, M.F., and Martin, J.F. (2003). Genetic dissection of Pitx2 in craniofacial development uncovers new functions in branchial arch morphogenesis, late aspects of tooth morphogenesis and cell migration. Development *130*, 6375-6385.

Liu, Z., Chen, Z., Shang, C., Yan, F., Shi, Y., Zhang, J., Qu, B., Han, H., Wang, Y., Li, D.*, et al.* (2017). IGF1-Dependent Synaptic Plasticity of Mitral Cells in Olfactory Memory during Social Learning. Neuron *95*, 106-122 e105.

Lui, J.H., Nguyen, N.D., Grutzner, S.M., Darmanis, S., Peixoto, D., Wagner, M.J., Allen, W.E., Kebschull, J.M., Richman, E.B., Ren, J.*, et al.* (2021). Differential encoding in prefrontal cortex projection neuron classes across cognitive tasks. Cell *184*, 489-506 e426.

Ma, Y., Zhang, L., and Huang, X. (2017). Building Cre Knockin Rat Lines Using CRISPR/Cas9. Methods Mol Biol *1642*, 37-52.

Masullo, L., Mariotti, L., Alexandre, N., Freire-Pritchett, P., Boulanger, J., and Tripodi, M. (2019). Genetically Defined Functional Modules for Spatial Orienting in the Mouse Superior Colliculus. Current biology : CB *29*, 2892-2904 e2898.

Matsuda, K., and Yuzaki, M. (2011). Cbln family proteins promote synapse formation by regulating distinct neurexin signaling pathways in various brain regions. The European journal of neuroscience *33*, 1447-1461.

Mayrhofer, J.M., El-Boustani, S., Foustoukos, G., Auffret, M., Tamura, K., and Petersen, C.C.H. (2019). Distinct Contributions of Whisker Sensory Cortex and Tongue-Jaw Motor Cortex in a Goal-Directed Sensorimotor Transformation. Neuron *103*, 1034-1043 e1035.

Moffitt, J.R., Bambah-Mukku, D., Eichhorn, S.W., Vaughn, E., Shekhar, K., Perez, J.D., Rubinstein, N.D., Hao, J., Regev, A., Dulac, C.*, et al.* (2018). Molecular, spatial, and functional single-cell profiling of the hypothalamic preoptic region. Science *362*.

572 Oliveira, A.F., and Yonehara, K. (2018). The Mouse Superior Colliculus as a Model System for Investigating Cell
573 Type-Based Mechanisms of Visual Motor Transformation. Frontiers in neural circuits *12*, 59.
574 Picelli, S., Faridani, O.R., Björklund, Å.K., Winberg, G., Sagasser, S., and Sandberg, R. (2014). Full-length RNA-seq
575 from single cells using Smart-seq2. Nature protocols *9*, 171-181.
576 Pouget, A., and Snyder, L.H. (2000). Computational approaches to sensorimotor transformations. Nature
577 neuroscience *3 Suppl*, 1192-1198.
578 Saunders, A., Macosko, E.Z., Wysoker, A., Goldman, M., Krienen, F.M., de Rivera, H., Bien, E., Baum, M., Bortolin, L.,
579 Wang, S.*, et al.* (2018). Molecular Diversity and Specializations among the Cells of the Adult Mouse Brain. Cell
580 *174*, 1015-1030 e1016.
581 Schiavo, G., Benfenati, F., Poulain, B., Rossetto, O., Polverino de Laureto, P., DasGupta, B.R., and Montecucco, C.
582 (1992). Tetanus and botulinum-B neurotoxins block neurotransmitter release by proteolytic cleavage of
583 synaptobrevin. Nature *359*, 832-835.
584 Seigneur, E., and Sudhof, T.C. (2018). Genetic Ablation of All Cerebellins Reveals Synapse Organizer Functions in
585 Multiple Regions Throughout the Brain. The Journal of neuroscience : the official journal of the Society for
586 Neuroscience *38*, 4774-4790.
587 Shah, S., Lubeck, E., Zhou, W., and Cai, L. (2016). In Situ Transcription Profiling of Single Cells Reveals Spatial
588 Organization of Cells in the Mouse Hippocampus. Neuron *92*, 342-357.
589 Shang, C., Chen, Z., Liu, A., Li, Y., Zhang, J., Qu, B., Yan, F., Zhang, Y., Liu, W., Liu, Z.*, et al.* (2018). Divergent
590 midbrain circuits orchestrate escape and freezing responses to looming stimuli in mice. Nature communications
591 *9*, 1232.
592 Shang, C., Liu, A., Li, D., Xie, Z., Chen, Z., Huang, M., Li, Y., Wang, Y., Shen, W.L., and Cao, P. (2019). A subcortical
593 excitatory circuit for sensory-triggered predatory hunting in mice. Nature neuroscience *22*, 909-920.
594 Shang, C., Liu, Z., Chen, Z., Shi, Y., Wang, Q., Liu, S., Li, D., and Cao, P. (2015). BRAIN CIRCUITS. A
595 parvalbumin-positive excitatory visual pathway to trigger fear responses in mice. Science *348*, 1472-1477.
596 Shapiro, E., Biezuner, T., and Linnarsson, S. (2013). Single-cell sequencing-based technologies will revolutionize
597 whole-organism science. Nat Rev Genet *14*, 618-630.
598 Sparks, D.L. (1986). Translation of sensory signals into commands for control of saccadic eye movements: role of
599 primate superior colliculus. Physiological reviews *66*, 118-171.
600 Stuart, T., Butler, A., Hoffman, P., Hafemeister, C., Papalexi, E., Mauck III, W.M., Hao, Y., Stoeckius, M., Smibert, P.,
601 and Satija, R. (2019). Comprehensive integration of single-cell data. Cell *177*, 1888-1902. e1821.
602 Tang, F., Barbacioru, C., Wang, Y., Nordman, E., Lee, C., Xu, N., Wang, X., Bodeau, J., Tuch, B.B., Siddiqui, A.*, et al.*
603 (2009). mRNA-Seq whole-transcriptome analysis of a single cell. Nature methods *6*, 377-382.
604 Tasic, B., Yao, Z., Graybuck, L.T., Smith, K.A., Nguyen, T.N., Bertagnolli, D., Goldy, J., Garren, E., Economo, M.N.,
605 Viswanathan, S.*, et al.* (2018). Shared and distinct transcriptomic cell types across neocortical areas. Nature *563*,
606 72-78.
607 Tervo, D.G., Hwang, B.Y., Viswanathan, S., Gaj, T., Lavzin, M., Ritola, K.D., Lindo, S., Michael, S., Kuleshova, E., Ojala,
608 D.*, et al.* (2016). A Designer AAV Variant Permits Efficient Retrograde Access to Projection Neurons. Neuron *92*,
609 372-382.
610 Vong, L., Ye, C., Yang, Z., Choi, B., Chua, S., Jr., and Lowell, B.B. (2011). Leptin action on GABAergic neurons
611 prevents obesity and reduces inhibitory tone to POMC neurons. Neuron *71*, 142-154.

612 Waite, M.R., Skidmore, J.M., Micucci, J.A., Shiratori, H., Hamada, H., Martin, J.F., and Martin, D.M. (2013).
613 Pleiotropic and isoform-specific functions for Pitx2 in superior colliculus and hypothalamic neuronal
614 development. Molecular and cellular neurosciences *52*, 128-139.
615 Wang, L., Liu, M., Segraves, M.A., and Cang, J. (2015). Visual Experience Is Required for the Development of Eye
616 Movement Maps in the Mouse Superior Colliculus. The Journal of neuroscience : the official journal of the
617 Society for Neuroscience *35*, 12281-12286.
618 Wang, L., McAlonan, K., Goldstein, S., Gerfen, C.R., and Krauzlis, R.J. (2020a). A Causal Role for Mouse Superior
619 Colliculus in Visual Perceptual Decision-Making. The Journal of neuroscience : the official journal of the Society
620 for Neuroscience *40*, 3768-3782.
621 Wang, L., Sarnaik, R., Rangarajan, K., Liu, X., and Cang, J. (2010). Visual receptive field properties of neurons in the
622 superficial superior colliculus of the mouse. The Journal of neuroscience : the official journal of the Society for
623 Neuroscience *30*, 16573-16584.
624 Wang, Q., Ding, S.-L., Li, Y., Royall, J., Feng, D., Lesnar, P., Graddis, N., Naeemi, M., Facer, B., and Ho, A. (2020b).
625 The Allen mouse brain common coordinate framework: a 3D reference atlas. Cell *181*, 936-953. e920.
626 Wei, P., Liu, N., Zhang, Z., Liu, X., Tang, Y., He, X., Wu, B., Zhou, Z., Liu, Y., Li, J.*, et al.* (2015). Processing of visually
627 evoked innate fear by a non-canonical thalamic pathway. Nature communications *6*, 6756.
628 Wickersham, I.R., Finke, S., Conzelmann, K.K., and Callaway, E.M. (2007). Retrograde neuronal tracing with a
629 deletion-mutant rabies virus. Nature methods *4*, 47-49.
630 Wilson, J.J., Alexandre, N., Trentin, C., and Tripodi, M. (2018). Three-Dimensional Representation of Motor Space in
631 the Mouse Superior Colliculus. Current biology : CB *28*, 1744-1755 e1712.
632 Wolock, S.L., Lopez, R., and Klein, A.M. (2019). Scrublet: computational identification of cell doublets in single-cell
633 transcriptomic data. Cell systems *8*, 281-291. e289.
634 Wu, Y.E., Pan, L., Zuo, Y., Li, X., and Hong, W. (2017). Detecting Activated Cell Populations Using Single-Cell
635 RNA-Seq. Neuron *96*, 313-329 e316.
636 Yilmaz, M., and Meister, M. (2013). Rapid innate defensive responses of mice to looming visual stimuli. Current
637 biology : CB *23*, 2011-2015.
638 Zeisel, A., Hochgerner, H., Lonnerberg, P., Johnsson, A., Memic, F., van der Zwan, J., Haring, M., Braun, E., Borm,
639 L.E., La Manno, G.*, et al.* (2018). Molecular Architecture of the Mouse Nervous System. Cell *174*, 999-1014
640 e1022.
641 Zheng, G.X., Terry, J.M., Belgrader, P., Ryvkin, P., Bent, Z.W., Wilson, R., Ziraldo, S.B., Wheeler, T.D., McDermott,
642 G.P., and Zhu, J. (2017). Massively parallel digital transcriptional profiling of single cells. Nature
643 communications *8*, 1-12.
644 Zhong, S., Ding, W., Sun, L., Lu, Y., Dong, H., Fan, X., Liu, Z., Chen, R., Zhang, S., Ma, Q.*, et al.* (2020). Decoding the
645 development of the human hippocampus. Nature *577*, 531-536.
646 Zhong, S., Zhang, S., Fan, X., Wu, Q., Yan, L., Dong, J., Zhang, H., Li, L., Sun, L., Pan, N.*, et al.* (2018). A single-cell
647 RNA-seq survey of the developmental landscape of the human prefrontal cortex. Nature *555*, 524-528.
648 Zhou, Z., Liu, X., Chen, S., Zhang, Z., Liu, Y., Montardy, Q., Tang, Y., Wei, P., Liu, N., Li, L.*, et al.* (2019). A VTA
649 GABAergic Neural Circuit Mediates Visually Evoked Innate Defensive Responses. Neuron *103*, 473-488 e476.

650

651

652

653 # METHODS

654 ## Animals

655 All experimental procedures were conducted following protocols approved by the
656 Administrative Panel on Laboratory Animal Care at the National Institute of Biological
657 Sciences, Beijing (NIBS) and Institute of Biophysics, Chinese Academy of Sciences. The
658 *Pitx2-Cre* knock-in line (Liu et al., 2003) was imported from the Mutant Mouse Resource
659 Centers (MMRRC_000126-UCD). The vGlut2-IRES-Cre (Vong et al., 2011) was
660 imported from the Jackson Laboratory (JAX Mice and Services). Mice were maintained
661 on a circadian 12-h light/12-h dark cycle with food and water available ad libitum. Mice
662 were housed in groups (3–5 animals per cage) before they were separated three days
663 prior to virus injection. After virus injection, each mouse was housed in one cage for
664 three weeks before subsequent experiments. To avoid potential sex-specific differences,
665 we used male mice only.

666 ## Nuclei preparation

667 Mice were anesthetized with 3% isoflurane and brains were removed and placed into
668 ice-cold oxygenated aCSF. SC were dissected from the midbrain and placed into
669 RNAlater (Invitrogen, AM7021) and stored at 4℃ overnight. To ensure the quality of the
670 experiment, two replicates were conducted and 5 mice were used for each replicate. On
671 the day for the experiment, tissue samples were washed with PBS (gibco, REF
672 10010-023) and cut into pieces <1 mm and were homogenized using a glass dounce
673 tissue grinder (Sigma, Cat #D8938) in 2 ml of ice-cold EZ PREP (Sigma, Cat #NUC-101).
674 Then the nuclei suspension was transferred into a 15 ml tube and incubated on ice for 5
675 minutes with 2 ml of ice-cold EZ PREP added. After incubation, the nuclei were
676 centrifuged at 500 x g for 5 minutes at 4℃. The nuclei were re-suspended with 4 ml

677 ice-cold EZ PREP and incubated on ice for another 5 minutes. Then the nuclei were
678 centrifuged at 500 x g for 5 minutes at 4℃ and washed in 4 ml Nuclei Suspension Buffer
679 (NBS; consisting of 1× PBS, 0.04% BSA and 0.1% RNase inhibitor (Clontech, Cat
680 #2313A)). After being re-suspended in 2 ml NBS, the nuclei were filtered with a 35-um
681 cell strainer (Corning, Cat #352235). The nuclei density was adjusted to 1,000,000
682 nuclei/ ml and placed on ice for use.

683 **Single-nuclei RNA-sequencing library construction**

684 Libraries were prepared using 10X GENOMICS platform following the RNA library
685 preparation protocols. Briefly, by using the 10x GemCode Technology, thousands of
686 nuclei were partitioned into nanoliter-scale Gel BeadIn-EMulsions (GEMs). At this step,
687 all the cDNA produced from the same nuclei were labeled by a common 10x Barcode.
688 Primers containing an Illumina R1 sequence (read1 sequencing primer), a 16-bp 10x
689 Barcode, a 10-bp randomer and a poly-dT primer sequence were released and mixed
690 with nuclei lysate and Master Mix upon dissolution of the single cell 3′ gel bead in a GEM.
691 The GEMs were incubated to generate barcoded, full-length cDNA from poly-adenylated
692 mRNA by reverse-transcription. After breaking the GEMs, silane magnetic beads were
693 used to remove the leftover biochemical reagents and primers. Before constructing the
694 library, the cDNA amplicon size was optimized by enzymatic fragmentation and size
695 selection. During the end repair and adaptor ligation step, P5, P7, a sample index and
696 R2 (read 2 primer sequence) were added to each selected cDNA. P5 and P7 primers
697 were used in Illumina bridge amplification of the cDNA (http://10xgenomics.com). The
698 libraries were sequenced using the Illumina HiSeq4000 with150-bp paired-end reads.

699 **High-throughput snRNA-seq data preprocessing and analyzing**

700 For 10X snRNA-seq data, the reads were aligned to mouse reference genome mm10
701 with Cell Ranger (v3.0.2) (Zheng et al., 2017). To detect potential doublets, we
702 performed the scrublet (version 0.2.1) pipeline on each sample with parameters
703 (expected_doublet_score=0.06, sim_doublet_ratio=20, min_gene_variability_pctl=85

and n_prin_comps=30) (Wolock et al., 2019). 1708/17979 cells with computed doublet score greater than 0.16 were identified as doublets and excluded from subsequent analysis. Next, a series of quality control analyses were performed. Cells with nGenes (number of detected genes) below 800 or above 6000 were discarded; Cells with nUMI above 20000 or percentage of mitochondrial genes greater than 3% were removed. Genes that didn't show expression in at least 3 cells were excluded. After quality control, 14892 cells and 23076 genes were kept for downstream analysis.

The downstream analysis of 10X snRNA-seq data was performed with R package Seurat (3.1.0) (Butler et al., 2018; Stuart et al., 2019). Briefly, A Seurat object was created with the filtered read counts. The log-transformation was then performed with the function NormalizeData. Next, 2000 variable genes were identified with function FindVariableGenes and passed to function RunPCA for the principal component analysis (PCA). Then, batch effect correction was performed using function fastMNN (Haghverdi et al., 2018) followed by dimension reduction with t-distributed stochastic neighbor embedding (t-SNE) approach using function RunTSNE. Subsequently, clustering analysis was performed with function FindClusters by setting parameter resolution to 2.0. Known markers *Slc17a6*, *Gad1*, *Mbp, Pdgfra*, *Aldh1a1*, *Cx3cr1*, *Cldn5*, *Foxc1* and *Ccdc146* were used to name the major cell types excitatory neurons, inhibitory neurons, oligodendrocytes, OPCs, astrocytes, microglia cells, endothelial cells, meninges and ciliated cells, respectively. In addition, we further sub-clustered excitatory neurons and inhibitory neurons into 9 and 10 subclusters, respectively, following the same procedure described above.

Allen brain in situ data processing and layer specificity score calculation with computational method (SPACED)

To determine whether different SC neuronal subtypes own spatial layer specificity, we analyzed the in-situ hybridization images of genes that are subtype specific from Allen Mouse Brain Atlas (https://mouse.brain-map.org/search/index) followed the

computational method SPACED. Briefly, the differentially expressed genes (DEGs) of excitatory neuron and inhibitory neuron subtypes were firstly computed. To access genes whose expression pattern is more subtype restricted, we computed subtype specificity score for each gene based on Jensen-Shannon divergence, inspired by Cusanovich's study (Cusanovich et al., 2018) and ranked the DEGs by their subtype specificity score. Then, for each neuron subtype, the top10 most subtype specific genes were selected as reference for spatial classification. The in-situ slices of the selected genes used for spatial classification were downloaded from Allen Mouse Brain Atlas (https://mouse.brain-map.org/search/index). After that, the color type of these slices was transformed into 8-bit using ImageJ (v1.48h3). The signal pixels of each slice were converted into red by performing 'Image>Adjust>Threshold' in ImageJ. Subsequently, the four layers of the superior colliculus, named as Superficial layer (SuG), Optic layer (Op), Intermediate Gray layer/Intermediate White layer (InG/InWh) and Deep Gray layer (DpG) were selected using ROI manager. In each slice, a region with the weakest signal was selected as the background. The signal intensity of the four layers were calculated respectively. Briefly, the area fraction (definition from ImageJ: The percentage of pixels in the image or selection that have been highlighted in red using Image>Adjust>Threshold. For non-thresholded images, the percentage of non-zero pixels.) of each of the five ROIs in each slice was firstly calculated. The signal intensity was then carried out by subtracting the area fraction of the background ROI (ROI with the weakest signal) from that of the other four ROIs (SuG, Op, InG/InWh and DpG). Afterwards, the computed in-situ signal intensities of each gene for the four SC layers were normalized into range 0 and 1. We then computed a log-transformation of the mean of signal intensity for each layer across the selected genes as the layer specificity score for the corresponding layer. To access the spatial distribution priority of each subtype, ANOVA analysis and post hoc test were performed on the processed signal intensities and p-value < 0.05 was considered as statistically significant. Source code for the computational method

758 SPACED is available at https://github.com/xiaoqunwang-lab/SPACED.

759 **Slice preparation and cell harvesting using patch-seq**

760 After anesthetized with 3% isoflurane, the mice were decapitated and the brains were
761 removed and placed into ice-cold oxygenated sucrose-based artificial cerebrospinal fluid
762 (sucrose-aCSF) containing (in mM): 234 Sucrose, 2.5 KCl, 1.25 NaH2PO4, 10 MgSO4,
763 0.5, CaCl2, 26 NaHCO3, and 11 D-glucose, pH 7.4. Brains were cut into 200 um thick
764 slices in ice-cold oxygenated sucrose-aCSF with a microtome (Leica VT 1200S). Then
765 the slices were incubated in oxygenated artificial cerebrospinal fluid (aCSF) containing
766 (in mM): 126 NaCl, 3 KCl, 26 NaHCO3, 1.2 NaH2PO4, 10 D-glucose, 2.4 CaCl2, and 1.3
767 MgCl2, pH 7.4 at room temperature for 1 hour. To pick the fluorescence labeled neurons
768 in SC, glass capillaries (2.0 mm OD, 1.16 mm ID, Sutter Instruments) were autoclaved
769 prior to pulling patch-seq pipettes. All the surfaces of the environment were kept clean
770 and RNase-free with DNA-OFF (Takara Cat. #9036) and RNase Zap (Life Technologies
771 Cat. #AM9780). To ensure a successful harvest of the cell, the patch-seq pipettes were
772 pulled by a micropipette puller (Sutter Instrument, MODEL P-97) until the resistance was
773 2-4 MΩ. The pipette solution containing 123 mM potassium gluconate, 12 mM KCl, 10
774 mM HEPES, 0.2 mM EGTA, 4 mM MgATP, 0.3 mM NaGTP, 10 mM sodium
775 phosphocreatine, 20 μg/ml glycogen, and 1 U/μl recombinant RNase inhibitor (Takara
776 Cat.no. 2313A), pH ~7.25 was prepared. Cells were absorbed into patch-seq pipettes
777 filled with pipette solution and ejected into RNase-free PCR tube containing 4ul of
778 RNase-free lysis buffer consisting of: 0.1% Triton X-100, 5 mM (each) dNTPs, 2.5 μM
779 Oligo-dT30, 1 U/μl RNase inhibitor, and ERCC RNA Spike-In Mix (Life Technologies Cat.
780 #4456740)(Cadwell et al., 2016a).

781 **Patch-seq library construction and sequencing**

782 The RNA collected from neurons by patch-seq were converted to DNA with the
783 Smart-seq2 protocol (Picelli et al., 2014). Briefly, reverse transcription of the
784 poly(A)-tailed mRNA with SuperScript II reverse transcriptase (Invitrogen REF

18064-014) was carried out. After 20 cycles of amplification, about 50 to 100 ng cDNA were produced. 25 ng cDNA was used as input DNA to construct the library with KAPA HyperPlus Kit (KAPABIOSYSTEM, KK8514). Briefly, the cDNA were fragmented with fragmentation enzymes for 20 minutes at 37 ℃. Then the fragmented cDNA were proceeded to end repair and A-tailing at 65 ℃ for 30 minutes. After adaptor ligation step, the cDNA were amplified with 6 to 8 cycles to produce enough library DNA for sequencing. The libraries were sequenced using Illumina HiSeq 2000.

Patch-seq data preprocessing and analyzing

Adapter and low-quality reads were discarded with Python script AfterQC (Chen et al., 2017). Paired-end reads were aligned to the mouse reference genome mm10 using software STAR (STAR 2.5.3a) (Dobin et al., 2013) with default parameters except for the use of setting output type (--outSAMtype). Reads were then counted with featureCounts (featureCounts 1.5.3) (Liao et al., 2014). Cells with nGene between 200 and 10000, percentage of mitochondrial genes lower than 10% and percentage of ERCC below 5% were included. Genes that have expression in at least two cells were included. The filtered counts contained then 60 cells and 19541 genes. The downstream analysis for Smart-seq data was carried out with R package Seurat (Butler et al., 2018; Stuart et al., 2019). Gene expression normalization was performed with function NormalizeData followed by computing variable genes using function FindVariableGenes. For dimensionality reduction, principal component analysis (PCA) and t-distributed Stochastic Neighbor Embedding (t-SNE) approaches were applied with function RunPCA and RunTSNE, respectively. Clustering analysis was done with FindClusters function by setting resolution to 1.

Mapping patch-seq data on high-throughput snRNA-seq data

To mapping Smart-seq clusters onto 10x clusters, we first performed CCA alignment with Seurat functions FindIntegrationAnchors and IntegrateData (Butler et al., 2018; Stuart et al., 2019) on these two datasets to remove potential technical batch effect. We

then computed the correlation coefficient between Smart-seq and 10x clusters based on the CCA integrated data.

Identification of differentially expressed genes

For 10X high-throughput snRNA data, differentially expressed genes were computed using FindAllMarkers function (Butler et al., 2018; Stuart et al., 2019) with method Wilcox. Genes with adjusted $P_{adj} < 0.05$ were identified as differentially expressed genes (DEGs). For smart-seq data, differentially expressed genes were computed using FindAllMarkers function with method roc. Genes with a power > 0.4 were identified as DEGs.

Tissue preparation and two-photon imaging

In AAV tracing experiments, brains were harvested four weeks after viral injection, post-fixed in 4% paraformaldehyde at 4℃ overnight (12-14 hours), rinsed in phosphate buffered saline for 15 min three times, and sliced into series of 120um thick coronal sections with a vibratome (Leica VT1200S, Leica). Complete tissue sections were scanned using 25X water-immersion objectives on a two-photon microscope (Nikon). Sections were imaged with 920nm excitation wavelengths. Z-series images were taken at 2um steps. Threshold parameters were individually adjusted for each case using the ImageJ (v1.53c).

Morphological connectivity reconstruction by image tracing of individual cells (M-CRITIC)

The dendrites and/or axons were traced using the ImageJ plug-in Simple Neurite Tracer (semiautomatic tracing) and the tracing results were saved in SWC format. Full anatomical morphology of individual neuron was reconstructed from a serial of aligned image-tracing stacks by manual works and custom written MATLAB (Mathworks, Natick, MA, R2019b) program (https://github.com/xiaoqunwang-lab/M-CRITIC). Subsequently, reconstructions of neuron morphology were registered to the Allen Mouse Common Coordinate Framework (CCF) (Wang et al., 2020b). Two experienced individuals performed back-to-back manual validation of the registration results.

839 **Generation of Cbln2-IRES-Cre mice**

840 The Cbln2-IRES-Cre mice were produced using CRISPR/Cas9 system based on the
841 method described before (Ma et al., 2017). In brief, two sgRNA targeting sites A
842 (Sequence: GGAGAAGAGAACAGAAGGTG) and B (Sequence:
843 GAGCCACCAGGATGATGGGA) were used for Cbln2 targeting. All homologous
844 recombination donor templates were prepared on the basis of the mice genomic
845 sequence (AssemblyGRCm38.p6) by insertion of IRES-Cre sequence to the end of each
846 targeting gene. The transcribed sgRNA and purified donor templates were mixed with
847 Cas9 protein for mice embryo microinjection. The new born pup genomic DNA was
848 extracted from 7-day-old mice tail based on the method described before (Ma et al.,
849 2017). Genotyping was performed using primers listed in Table S6. The correct insertion
850 was further confirmed by sequencing.

851 **AAV vectors**

852 The AAV serotype used in the present study is AAV2/9. The AAVs used in the present
853 study are listed in Table S6. AAV-EF1α-DIO-EGFP-2A-TeNT was from Thomas Südhof
854 Lab at Stanford University. The plasmid for pAAV-EF1α-DIO-ChR2-mCherry (Addgene
855 #20297) was from Deisseroth Lab. The cDNA for AAV-EF1α-DIO-jGCaMP7s was from
856 Kim Lab (Addgene #104463). The viral particles were prepared by Taitool Inc. and
857 BrainVTA Inc. The produced viral vector titers before dilution were in the range of
858 0.8-1.5×10^{13} viral particles/ml. The final titer used for AAV injection is 5×10^{12} viral
859 particles/ml.

860 **Stereotaxic injection**

861 Mice were anesthetized with an intraperitoneal injection of tribromoethanol (125–250
862 mg/kg). Standard surgery was performed to expose the brain surface above the superior
863 colliculus (SC), zona incerta (ZI), and lateral posterior thalamic nucleus (LPTN).

Coordinates used for SC injection were: bregma -3.80 mm, lateral ± 1.00 mm, and dura -1.25 mm. Coordinates used for ZI injection were: bregma -2.06 mm, lateral ± 1.25 mm, and dura -4.00 mm. Coordinates used for LPTN injection were: bregma -2.30 mm, lateral ± 1.50 mm, and dura -2.30 mm. The injection was performed with the pipette connected to a Nano-liter Injector 201 (World Precision Instruments, Inc.) at a slow flow rate of 0.15 μl / min to avoid potential damage to local brain tissue. The pipette was withdrawn at least 20 min after viral injection. For optogenetic activation and fiber photometry experiments, AAV injections were unilateral and were followed by ipsilateral optical fiber implantation (see "Optical fiber implantation"). For TeNT-mediated synaptic inactivation experiments, AAV injections were bilateral.

Optical fiber implantation

Thirty minutes after the AAV injection, a ceramic ferrule with an optical fiber (230 μm in diameter, N.A. 0.37) was implanted with the fiber tip on top of the Cbln2+ SC neurons (bregma -3.80 mm, lateral +0.75 mm, and dura -1.00 mm) or Pitx2+ SC neurons (bregma -3.80 mm, lateral +1.75 mm, and dura -1.75 mm). In some cases, the optical fiber was implanted with the fiber tip on top of the ZI (bregma -2.06 mm, lateral +1.25 mm, dura -4.00 mm) or LPTN (bregma -2.30 mm, lateral +1.50 mm, dura -2.30 mm). The ferrule was then secured on the skull with dental cement. After implantation, the skin was sutured, and antibiotics were applied to the surgical wound. The optogenetic and fiber photometry experiments were conducted at least three weeks after optical fiber implantation. All experimental designs related to optical fiber implantation are summarized in Table S7. For optogenetic stimulation, the output of the laser was measured and adjusted to 5, 10, 15 and 20 mW before each experiment. The pulse onset, duration, and frequency of light stimulation were controlled by a programmable pulse generator attached to the laser system. After AAV injection and fiber implantation, the mice were housed individually for three weeks before the behavioral tests.

Preparation of the behavioral tests

Before the behavioral tests, the animals were handled daily by the experimenters for at least three days. On the day of the behavioral test, the animals were transferred to the testing room and were habituated to the room conditions for 3 h before the experiments started. The apparatus was cleaned with 20% ethanol to eliminate odor cues from other animals. All behavioral tests were conducted during the same circadian period (13:00–19:00). All behaviors were scored by the experimenters, who were blind to the animal treatments.

Visually-evoked freezing response

Visually-evoked freezing response was measured according to the established behavioral paradigm in a standard arena (35 cm × 35 cm square open field) with regular mouse bedding. A regular computer monitor was positioned above the arena for presentation of overhead moving visual target. After entering, the mice were allowed to explore the arena for 10 min. This was followed by the presentation of a small visual target moving overhead. The visual target was a black circle (2.5 cm in diameter), which was 5 deg of visual angle, moving in a linear trajectory at 10 cm/s from one corner to the other of the monitor. The luminance of the black circle and the grey background was 0.1 and 3.6 cd m^{-2}, respectively. Mouse behavior was recorded (25 fps) by two orthogonally positioned cameras with LEDs providing infrared illumination. The location of the mouse in the arena (X, Y) was measured by a custom-written Matlab program described previously (Shang et al., 2018). The instantaneous locomotion speed was calculated with a 200 ms time-bin. To quantitatively measure the freezing response, we calculated the average locomotion speed before (3 s), average speed during (5 s), and average speed after (5 s) visual stimuli.

For testing optogenetically-evoked freezing response, a 473-nm diode pumped solid state (DPSS) laser system was used to generate the 473-nm blue laser for light stimulation. A FC/PC adaptor was used to connect the output of the laser to the implanted ferrule for intracranial light delivery. The mice were handled daily with all optics connected for at least three consecutive days before the behavioral test to reduce stress and anxiety. Before each experiment, the output of the laser was adjusted to 5 mW. The pulse onset, duration, and frequency of light stimulation were controlled by a programmable pulse generator attached to the laser system. Locomotor behaviors before, during and after light stimulation (10 Hz, 20 ms, 5 mW, 5 s) were recorded with two orthogonally positioned cameras and were measured by a custom-written Matlab program described previously (Shang et al., 2018).

Behavioral paradigm for predatory hunting

The procedure of predatory hunting experiment was described previously (Shang et al., 2019). Before the predatory hunting test, the mice went through a 9-day habituation procedure (Day H1–H9). On each of the first three habituation days (Day H1, H2, H3), three cockroaches were placed in the home-cage (with standard chow) of mice at 2:00 PM. The mice readily consumed the cockroaches within 3 h after cockroach appearance. On Day H3, H5, H7, and H9, we initiated 24-h food deprivation at 7:00 PM by removing chow from the home-cage. On Day H4, H6, and H8 at 5:00 PM, we let the mice freely explore the arena (25 cm x 25 cm) for 10 min, followed by three trials of hunting practice for the cockroach. After hunting practice, we put the mice back in their home-cages and returned the chow at 7:00 PM. On the test day, we let the mice freely explore the arena for 10 min, followed by three trials of predatory hunting. After the tests, the mice were put back in their home-cage, followed by the return of chow. The cockroach was purchased from a merchant in Tao-Bao Online Stores (www.taobao.com).

Before the hunting practice or test, the mice were transferred to the testing room and habituated to the room conditions for 3 h before the experiments started. The arena was cleaned with 20% ethanol to eliminate odor cues from other mice. All behaviors were scored by the experimenters, who were blind to the animal treatments. Hunting behaviors were measured in an arena (25 cm × 25 cm, square open field) without regular mouse bedding. After entering, the mice explored the arena for 10 min, followed by the introduction of a cockroach. For each mouse, predatory hunting was repeated for three trials. Each trial began with the introduction of prey to the arena. The trial ended when the predator finished ingesting the captured prey. After the mice finished ingesting the prey body, debris was removed before the new trial began.

Measurement of predatory attack in predatory hunting

In the paradigm of predatory hunting, mouse behavior was recorded in the arena with three orthogonally positioned cameras (50 frames/sec; Point Grey Research, Canada). With the video taken by the overhead camera, the instantaneous head orientation of predator relative to prey (azimuth angle) and predator-prey distance (PPD) was analyzed with theSoftware EthoVision XT 14 (Noldus Information Technology). With the videos taken by the two horizontal cameras, predatory attacks with jaw were visually identified by replaying the video frame by frame (50 frames/sec). We marked the predatory jaw attacks with yellow vertical lines in the behavioral ethogram of predatory hunting. With this method, we measured three parameters of predatory hunting: time to capture, latency to attack, and attack frequency. Time to capture was defined as the time between the introduction of prey and the last jaw attack. Latency to attack was defined as the time between the introduction of the prey and the first jaw attack from the predator. Attack frequency was defined as the number of jaw attacks divided by time to prey capture. Data for three trials were averaged.

Fiber photometry recording

A fiber photometry system (ThinkerTech, Nanjing, China) was used for recording GCaMP signals from genetically identified neurons. To induce fluorescence signals, a laser beam from a laser tube (488 nm) was reflected by a dichroic mirror, focused by a 10× lens (N.A. 0.3) and coupled to an optical commutator. A 2-m optical fiber (230 μm in diameter, N.A. 0.37) guided the light between the commutator and implanted optical fiber. To minimize photo bleaching, the power intensity at the fiber tip was adjusted to 0.02 mW. The GCaMP7s (Dana et al., 2019) fluorescence was band-pass filtered (MF525-39, Thorlabs) and collected by a photomultiplier tube (R3896, Hamamatsu). An amplifier (C7319, Hamamatsu) was used to convert the photomultiplier tube current output to voltage signals, which were further filtered through a low-pass filter (40 Hz cut-off; Brownlee 440). The analogue voltage signals were digitalized at 100 Hz and recorded by a Power 1401 digitizer and Spike2 software (CED, Cambridge, UK).

AAV-hSyn-DIO-jGCaMP7s was stereotaxically injected into the SC of *Cbln2-IRES-Cre* mice or *Pitx2-Cre* mice followed by optical fiber implantation above the Cbln2+ SC neurons or Pitx2+ SC neurons (see “Stereotaxic injection” and “Optical fiber implantation”). Three weeks after AAV injection, fiber photometry was used to record GCaMP signals from the Cbln2+ SC neurons or Pitx2+ SC neurons of head-fixed mice standing on a treadmill in response to visual and vibrissal somatosensory stimuli (see below). A flashing LED triggered by a 1-s square-wave pulse was simultaneously recorded to synchronize the video and GCaMP signals. After the experiments, the optical fiber tip sites in the SC were histologically examined in each mouse.

Visual stimulation

The test mice were head-fixed and standing on top of a cylindrical treadmill (Nanjing Thinktech Inc.) for fiber photometry recording of SC neurons in response to visual stimuli. The contralateral eye was kept open, and the ipsilateral eye was covered to prevent viewing. A 45-cm wide and 35-cm high screen was placed 18 cm from the contralateral

eye and 25° to the mid-sagittal plane of the mouse, resulting in a visually stimulated area (100° horizontal × 90° vertical) in the lateral visual field. The orientation of the screen was adjusted ~45° to make the screen perpendicular to the eye axis of the contralateral eye. After identification of the receptive field location on the screen of SC neurons, a computer-generated black circle (diameter= 5° or 25°) moving across the visual receptive field in eight direction at different speed (32°/s or 128°/s) was presented. The luminance of the black circle and grey background was 0.1 and 6.6 cd/m^2, respectively. The black circle first appeared stationary outside the receptive field for 2 s to collect baseline calcium signals as controls, and was then presented with an interval of at least 15 s between trials to allow the neurons to recover from any motion adaptation.

Vibrissal air-puff stimulation

To mimic the somatosensory cues of moving prey, brief air-puffs (50 ms) with different strengths (15 psi or 30 psi) were delivered through a metal tube (diameter 1.5 mm) connected with Picospritzer III. The output of Picospritzer III was controlled by a programmable pulse generator. When delivering air-puffs as vibrissal somatosensory stimuli, the tube was oriented from temporal to nasal side of mouse. The distance between the tube nozzle and the whiskers were ~30 mm. When presenting repetitive air-puff stimuli, the frequency was either 0.5 Hz or 2 Hz. For each mouse, 10-15 trials were repeatedly presented to the whiskers, so that an average response was obtained.

Cell-type-specific anterograde tracing

For cell-type-specific anterograde tracing of Cbln2+ and Pitx2+ SC neurons, AAV-DIO-EGFP (200 nano litter) was stereotaxically injected into the SC of Cbln2-IRES-Cre and Pitx2-Cre mice, respectively. The mice were then maintained in a cage individually. Three weeks after viral injection, mice were perfused with saline followed by 4% paraformaldehyde (PFA) in PBS. After 8 h of post-fixation in 4% PFA,

coronal or sagittal brain sections at 40 μm in thickness were prepared using a cryostat (Leica CM1900). All coronal sections were collected and stained with primary antibody against EGFP and DAPI. The coronal brain sections were imaged with an Olympus VS120 epifluorescence microscope (10× objective lens).

Cell-type-specific RV tracing

The modified rabies virus based three-virus system was used for mapping the whole-brain inputs to vGAT+ AHN neurons (Wickersham et al., 2007). All the viruses included AAV2/9-CAG-DIO-EGFP-2A-TVA (5 x 10^{12} viral particles/ml), AAV2/9-CAG-DIO-RG (5 x 10^{12} viral particles/ml), and EnvA-pseudotyped, glycoprotein (RG)-deleted and DsRed-expressing rabies virus (RV-EvnA-DsRed, RV) (5.0 × 10^{8} viral particles/ml), which were packaged and provided by BrainVTA Inc. (Wuhan, China). A mixture of AAV2/9-CAG-DIO-EGFP-2A-TVA and AAV2/9-CAG-DIO-RG (1:1, 200 nl) was stereotaxically injected into the SC of Cbln2-IRES-Cre or Pitx2-Cre mice unilaterally. Two weeks after AAV helper injection, RV-EvnA-DsRed (300 nl) was injected into the same location in the SC of Cbln2-IRES-Cre or Pitx2-Cre mice in a biosafety level-2 lab facility. Starter neurons were characterized by the coexpression of DsRed and EGFP, which were restricted in the SC.

One week after injection of rabies virus, mice were perfused with saline followed by 4% paraformaldehyde (PFA) in PBS. After 8 h of post-fixation in 4% PFA, coronal brain sections at 40 μm in thickness were prepared using a cryostat (Leica CM1950). All coronal sections were collected and stained with DAPI. The coronal brain sections were imaged with an Olympus VS120 epifluorescence microscope (10× objective lens) and analyzed with ImageJ. For quantifications of subregions, boundaries were based on the Allen Institute's reference atlas. We selectively analyzed the retrogradely labeled dense areas. The factional distribution of total cells labeled by rabies virus was measured.

Cell-counting strategies

Cell-counting strategies are summarized in Table S8. For counting cells in the SC, we collected coronal sections (40 μm) from bregma -3.08 mm to bregma -4.60 mm for each mouse. We acquired confocal images (20x objective, Zeiss LSM 780) followed by cell counting with ImageJ software. By combining fluorescent in situ hybridization and immunohistochemistry, we counted the number of Cbln2+ and Pitx2+ cells in the SC and calculated the percentages of Cbln2+ and Pitx2+ neurons in the neuronal population labeled by EGFP. To analyze monosynaptic inputs of Cbln2+ SC neurons, we counted DsRed+ cells in a series of brain areas. For the detailed information on the brain regions and cell counting strategy, see Table S8. We acquired fluorescent images (10x objective, Olympus) followed by cell counting with ImageJ software.

Slice physiological recording

Slice physiological recording was performed according to the published work (Liu et al., 2017). Brain slices containing the SC were prepared from adult mice anesthetized with Isoflurane before decapitation. Brains were rapidly removed and placed in ice-cold oxygenated (95% O_2 and 5% CO_2) cutting solution (228 mM sucrose, 11 mM glucose, 26 mM $NaHCO_3$, 1 mM NaH_2PO_4, 2.5 mM KCl, 7 mM $MgSO_4$, and 0.5 mM $CaCl_2$). Coronal brain slices (400 μm) were cut using a vibratome (VT 1200S, Leica Microsystems). The slices were incubated at 28°C in oxygenated artificial cerebrospinal fluid (ACSF: 119 mM NaCl, 2.5 mM KCl, 1 mM NaH_2PO_4, 1.3 mM $MgSO_4$, 26 mM $NaHCO_3$, 10 mM glucose, and 2.5 mM $CaCl_2$) for 30 min, and were then kept at room temperature under the same conditions for 1 h before transfer to the recording chamber at room temperature. The ACSF was perfused at 1 ml/min. The acute brain slices were visualized with a 40× Olympus water immersion lens, differential interference contrast (DIC) optics (Olympus Inc., Japan), and a CCD camera.

Patch pipettes were pulled from borosilicate glass capillary tubes (Cat #64-0793, Warner Instruments, Hamden, CT, USA) using a PC-10 pipette puller (Narishige Inc.,

Tokyo, Japan). For recording of action potentials (current clamp), pipettes were filled with solution (in mM: 135 K-methanesulfonate, 10 HEPES, 1 EGTA, 1 Na-GTP, 4 Mg-ATP, and 2% neurobiotin, pH 7.4). The resistance of pipettes varied between 3.0–3.5 MΩ. The voltage signals were recorded with MultiClamp 700B and Clampex 10 data acquisition software (Molecular Devices). After establishment of the whole-cell configuration and equilibration of the intracellular pipette solution with the cytoplasm, series resistance was compensated to 10–15 MΩ. Recordings with series resistances of > 15 MΩ were rejected. An optical fiber (200 μm in diameter) was used to deliver light pulses, with the fiber tip positioned 500 μm above the brain slices. Laser power was adjusted to 5 mW. Light-evoked action potentials from ChR2-mCherry^{+} neurons in the SC were triggered by a light-pulse train (473 nm, 2 ms, 10 Hz or 20 Hz, 20 mW) synchronized with Clampex 10 data acquisition software (Molecular Devices).

RNA in situ hybridization

Mice were perfused with PBS treated with 0.1% DEPC (Sigma, D5758), followed by DEPC-treated PBS containing 4% PFA (PBS-PFA). Brains were post-fixed in DEPC-treated PBS-PFA solution overnight and then placed in DEPC-treated 30% sucrose solution at 4℃ for 30h. Brain sections to a thickness of 30 μm were prepared using a cryostat (Leica, CM3050S) and collected in DPEC-treated PBS. Fluorescence in situ hybridization (FISH) was performed as previously described (Chen et al., 2020) with minor modifications. Briefly, brain sections were rinsed with DPEC-treated PBS, permeabilized with DPEC-treated 0.1% Tween 20 solution (in PBS) and DPEC-treated 2 × SSC containing 0.5% Triton. Brain sections were then treated with H2O2 solution and acetic anhydride solution to reduce nonspecific FISH signals. After 2h incubation in prehybridization buffer (50% formamide, 5 × SSC, 0.1% Tween20, 0.1% CHAPS, 5mM EDTA in DEPC-treated water) at 65℃, brain sections were then hybridized with the hybridization solution containing mouse anti-sense cRNA probes (digoxigenin labeling)

for Cbln2 (primers CAGCTTCCACGTGGTCAA and AGCCCCCAGCATGAAAAC) or Pitx2 (primers CTCTCAGAGTATGTTTTCCCCG and AGGATGGGTCGTACATAGCAGT) at 65°C for 20h.The sequences of cDNA primers for cRNA probes were the same as those in the ISH DATA of the Allen brain atlas (https://mouse.brain-map.org/). After washing, brain sections were incubated with Anti-Digoxigenin-POD, Fab fragments (1:400, Roche, 11207733910) at 4°C for 30 h, and FISH signals were detected using a TSA Plus Cyanine 3 kit (NEL744001KT, PerkinElmer). To visualized the GFP signals, brain sections were incubated with a primary antibody against GFP (1:2000, ab290, Abcam) at 4℃ for 24 h and then with an Alexa Fluor® 488-conjugated goat anti-rabbit secondary antibody (1:500, A11034, Invitrogen) at room temperature for 2h. Brain sections were mounted and imaged using a Zeiss LSM780 confocal microscope or the Olympus VS120 Slide Scanning System.

Immunohistochemistry

Mice were anesthetized with isoflurane and sequentially perfused with saline and phosphate buffered saline (PBS) containing 4% paraformaldehyde (PFA). Brains were removed and incubated in PBS containing 30% sucrose until they sank to the bottom. Post-fixation of the brain was avoided to optimize immunohistochemistry. Cryostat sections (40 μm) were collected, incubated overnight with blocking solution (PBS containing 10% goat serum and 0.7% Triton X-100), and then treated with primary antibodies diluted with blocking solution for 3–4 h at room temperature. Primary antibodies used for immunohistochemistry are displayed in Table S6. Primary antibodies were washed three times with washing buffer (PBS containing 0.7% Triton X-100) before incubation with secondary antibodies (tagged with Cy2, Cy3, or Cy5; dilution 1:500; Life Technologies Inc., USA) for 1 h at room temperature. Sections were then washed three times with washing buffer, stained with DAPI, and washed with PBS, transferred onto Super Frost slides, and mounted under glass coverslips with mounting media.

Sections were imaged with an Olympus VS120 epifluorescence microscope (10× objective lens) or a Zeiss LSM 710 confocal microscope (20× and 60× oil-immersion objective lens). Samples were excited by 488, 543, or 633 nm lasers in sequential acquisition mode to avoid signal leakage. Saturation was avoided by monitoring pixel intensity with Hi-Lo mode. Confocal images were analyzed with ImageJ software.

Data quantification and statistical analyses

All experiments were performed with anonymized samples in which the experimenter was unaware of the experimental conditions of the mice. For the statistical analyses of experimental data, Student t-test and One-Way ANOVA were used. The “n” used for these analyses represents number of mice or cells. See the detailed information of statistical analyses in figure legend and in Table S9. All statistical comparisons were conducted on data originating from three or more biologically independent experimental replicates. All data are shown as means ± SEM.

Data availability

The scRNA-seq data used in this study have been deposited in the Gene Expression Omnibus (GEO) under accession numbers GSE162404. The data that support the findings of this study are available from the corresponding author upon reasonable request.

FIGURE LEGENDS

Figure 1 Identification and characterization of cell types and spatial heterogeneity of mouse superior colliculus neurons

(A) Unbiased clustering of snRNA-seq data of mouse SC cells. Each dot represents an individual cell. The cells were grouped into 26 clusters, and the cell types were annotated according to the expression of known marker genes. **(B)** t-SNE showing the known markers of major cell types (excitatory neurons, inhibitory neurons, oligodendrocytes, OPCs, astrocytes, microglia, endothelial cells and meningeal cells) in the mouse SC. The scale bar indicates the relative gene expression level. (gray, low; red, high). **(C, D)** Dot plots showing the differentially expressed genes among 9 excitatory neuron subclusters (C) and 10 inhibitory neuron subclusters (D). **(E, F)** Spatial expression of the top DEGs of excitatory neuron subclusters (E) and inhibitory neuron subclusters (F). Upper panel: gene expression levels projected onto the two-dimensional t-SNE and colored according to relative gene expression level (gray, low; red, high). Red dashed line, excitatory neuron subclusters; blue dashed line, inhibitory neuron subclusters. Lower panel: In situ hybridization staining of mouse superior colliculus for the identified excitatory neuron layer markers (from the Allen Brain Atlas). **(G)** Heatmap showing the computed layer specificity score for each excitatory neuron subcluster (left) and each inhibitory neuron subcluster (right). Statistical analyses were performed by ANOVA (* $P<0.05$). **(H)** SC layer information annotation of neurons. Upper panel: cells colored by layer information as indicated by the legend on the bottom. Lower panel: gene ontology enrichment analysis of layer-annotated SC neurons.

Figure 2 Projection-based analyses of single-cell gene expression profiles

(A) Schematic diagram showing injection of AAV mixture into the SC of vGlut2-IRES-Cre mice for sparse labeling of glutamatergic SC neuron projections. **(B)** Two reconstructed neurons (blue, cells projected from the Op to the LPTN; brown, cells projected from the InG to the ZI) were registered to the mouse brain regions (Op, magenta; LPTN, orange; InG/InWh, green; ZI, cyan). **(C)** Coronal, sagittal and horizontal views of reconstructed neurons. Scale bar, 1 mm. **(D)** Schematic diagram showing injection of AAV2-retro-DIO-EGFP into the LPTN of vGlut2-IRES-Cre mice for labeling of LPTN-projecting glutamatergic SC neurons. **(E)** Sample micrograph showing the distribution of LPTN-projecting glutamatergic SC neurons labeled by EGFP. **(F)** Schematic diagram showing injection of AAV2-retro-DIO-EGFP into the ZI of vGlut2-IRES-Cre mice for labeling of ZI-projecting glutamatergic SC neurons. **(G)** Sample micrograph showing the distribution of ZI-projecting glutamatergic SC neurons labeled by EGFP. **(H)** Three-dimensional t-SNE plot showing SC cells sequenced by patch-seq. The cells are colored according to their cell projection identities (OP-LPTN, blue; InG-ZI, red). **(I)** Heatmap showing the differentially expressed genes of ZI- and LPTN-projecting SC neurons. The scale bar indicates the relative gene expression level. (**J)** Expression of genes enriched in LPTN-projecting and ZI-projecting neurons visualized as a t-SNE plot (blue, low; yellow, high). **(K)** Transcriptional correlation between LPTN-projecting and ZI-projecting neurons (patch-seq) and excitatory neuron subtypes (high-throughput snRNA-seq). The scale bar indicates the correlation coefficient (blue, low; yellow, high). **(L, M)** Volcano plot showing the differentially expressed genes in excitatory neuron subtypes Ex-3 and Ex-6 (L) and excitatory neuron subtypes Ex-1 and Ex-4 (M). Each dot represents a gene. Significantly upregulated genes are shown in green. **(N)** t-SNE plot visualizing the expression of differentially expressed genes in LPTN-projecting (top) and ZI-projecting (bottom) neurons in the same layout used in Figure 1A. The scale bar indicates the relative gene expression

1190 level (gray, low; red, high).

1191

Figure 3 Synaptic inactivation of Cbln2+ and Pitx2+ SC neurons

(A) Sample coronal section showing the restricted distribution of EGFP-expressing neurons in the Op layer of the SC in Cbln2-IRES-Cre mice. **(B)** Sample micrographs showing the specificity and efficiency of the Cbln2-IRES-Cre line for labeling of SC neurons expressing Cbln2 mRNA. **(C)** Schematic diagram showing the behavioral paradigm of the visually evoked freezing response in mice. **(D)** Time courses of locomotion speed before, during and after the sweep of an overhead moving visual target in mice without (Ctrl) or with (TeNT) synaptic inactivation of Cbln2+ SC neurons. **(E-G)** Quantitative analysis of locomotion speed before (E), during (F) and after (G) the sweep of an overhead moving target in mice without (Ctrl) and with (TeNT) synaptic inactivation of Cbln2+ SC neurons. **(H)** Sample coronal section showing the restricted distribution of EGFP-expressing neurons in the In layer of the SC in Pitx2-Cre mice. **(I)** Sample micrographs showing the specificity and efficiency of the Pitx2-Cre line for labeling of SC neurons expressing Pitx2 mRNA. **(J)** Schematic diagram showing the behavioral paradigm of predatory hunting in mice. **(K)** Behavioral ethograms of predatory hunting in mice without (Ctrl) and with (TeNT) synaptic inactivation of Pitx2+ SC neurons. The yellow vertical lines indicate jaw attacks. The PPD curve shows the time course of prey-predator distance. **(L-N)** Quantitative analysis of latency to attack (L), time to capture (M) and attack frequency (N) in mice without (Ctrl) and with (TeNT) synaptic inactivation of SC Pitx2+ neurons. The data in (D-G, L-N) are presented as mean ± SEM (error bars). The statistical analyses in (E-G, L-N) were performed using Student's t-test (n.s. $P>0.1$; *** $P < 0.001$). For the P values, see Table S9. Scale bars are indicated in the graphs.

Figure 4 Sensory responses of Cbln2+ and Pitx2+ SC neurons

(A, B) Sample micrographs showing the optical fiber tracks above GCaMP7-positive SC neurons in Cbln2-IRES-Cre (A) and Pitx2-Cre (B) mice. **(C)** Schematic diagram of the experimental configuration showing vibrissal tactile stimulation (air-puff) and visual stimulation; the latter was presented as a black circle moving across the receptive field (R.F.) on a tangent screen. **(D)** Normalized GCaMP fluorescence changes (ΔF/F) of Cbln2+ SC neurons in response to a stimulus consisting of a black circle (5°) moving at 32°/s in various directions (T-to-N, N-to-T, V-to-D, D-to-V). N, D, T and V indicate nasal, dorsal, temporal and ventral, respectively. **(E)** Normalized GCaMP fluorescence changes (ΔF/F) of Cbln2+ SC neurons in response to a black circle (5°) moving (T-to-N) at different velocities (32°/s and 128°/s). **(F)** Normalized GCaMP fluorescence changes (ΔF/F) of Cbln2+ SC neurons in response to black circles of different sizes (5° and 25°) moving in a T-to-N direction at 32°/s. **(G)** Normalized GCaMP fluorescence changes (ΔF/F) of Pitx2+ SC neurons in response to air puffs of different strengths (0, 10, 20, and 40 p.s.i.) directed toward the contralateral or ipsilateral vibrissal area. **(H)** Quantitative analysis of peak GCaMP responses of Cbln2+ SC neurons to black circles moving in eight directions. Inset, eight directions spaced by 45°. **(I)** Quantitative analysis of the peak GCaMP responses of Cbln2+ SC neurons to black circles moving at different velocities. **(J)** Quantitative analysis of the peak GCaMP responses of Cbln2+ SC neurons to moving black circles with different diameters. **(K)** Quantitative analysis of the peak GCaMP responses of Pitx2+ SC neurons to air puffs of different strengths directed toward the contralateral or ipsilateral vibrissal areas. The data in (D-K) are presented as mean ± SEM (error bars). The statistical analyses in (K) were performed by one-way ANOVA (*** $P < 0.001$). For the P values, see Table S9. Scale bars are indicated in the graphs.

Figure 5 Retrograde tracing of Cbln2+ and Pitx2+ SC neurons using rabies virus

(A) Series of schematic diagrams showing the strategy for monosynaptic retrograde tracing of Cbln2+ and Pitx2+ SC neurons using a combination of AAV and rabies virus (RV). Left, AAV helpers and RV used for injection. Middle, injection into the SC of Cbln2-IRES-Cre and Pitx2-Cre mice. Right, timing of AAV and RV injections. **(B, C)** Sample micrographs showing the expression of EGFP (green) and DsRed (red) in Cbln2+ and Pitx2+ neurons in the SC of Cbln2-IRES-Cre (B) and Pitx2-Cre mice (C). The dually labeled cells indicate starter cells. For single-channel images, see Figure S8. **(D-G)** Sample micrographs showing DsRed+ cells in various brain regions, including the contralateral and ipsilateral retina (D), the primary visual cortex (V1) (E), the contralateral principal trigeminal nucleus (Pr5) (F), and the ipsilateral primary somatosensory cortex (S1) (G), of Cbln2-IRES-Cre and Pitx2-Cre mice. **(H)** Fractional distribution of total DsRed-labeled cells in various brain regions that monosynaptically project to Cbln2+ and Pitx2+ SC neurons. The scale bars are labeled in the graphs. The number of mice (H) is indicated in each graph. The data in (H) are presented as mean ± SEM. The statistical analyses in (H) were performed using Student's t-test (*** $P < 0.001$). For the P values, see Table S9.

Figure 6 Anterograde tracing of Cbln2+ and Pitx2+ SC neurons

(A, B) Sample micrograph (left) and quantitative analysis (right) showing the distribution of EGFP-expressing neurons in the SC of Cbln2-IRES-Cre (A) and Pitx2-Cre mice (B). **(C)** Sample micrographs showing the distribution of EGFP-positive axons in the LPLR and LPMR (collectively the LPTN) of Cbln2-IRES-Cre (left) and Pitx2-Cre (right) mice. **(D)** Quantitative analysis of fluorescence signals from EGFP+ axons in the LPTN of Cbln2-IRES-Cre and Pitx2-Cre mice. **(E)** Sample micrographs showing the distribution of EGFP-positive axons in the ZI of Cbln2-IRES-Cre (left) and Pitx2-IRES-Cre (right) mice. **(F)** Quantitative analysis of fluorescence signals from EGFP+ axons in the ZI of Cbln2-IRES-Cre and Pitx2-Cre mice. **(G)** Schematic diagram showing the viral injection strategy used to label LPTN-projecting Cbln2+ SC neurons. **(H)** Coronal section from a Cbln2-IRES-Cre mouse showing the distribution of Cbln2+ SC neurons labeled by AAV2-retro-DIO-EGFP and AAV-DIO-mCherry. **(I)** Sample micrograph (left) and quantitative analysis (right) showing the number of LPTN-projecting Cbln2+ SC neurons (EGFP+) relative to total Cbln2+ SC neurons (mCherry+). **(J)** Schematic diagram showing the viral injection strategy used to label ZI-projecting Pitx2+ SC neurons. **(K)** Coronal section from a Pitx2-Cre mouse showing the distribution of Pitx2+ SC neurons labeled by AAV2-retro-DIO-EGFP and AAV-DIO-mCherry. **(L)** Sample micrograph (left) and quantitative analysis (right) showing the number of ZI-projecting Pitx2+ SC neurons (EGFP+) relative to total Pitx2+ SC neurons (mCherry+). The data in A, B, D, F, I, and L are presented as mean ± SEM (error bars). The statistical analyses in D and F were performed using Student's t-test (*** $P < 0.001$). For the P values, see Table S9. Scale bars are indicated in the graphs.

Figure 7 Activation of the Cbln2+ SC-LPTN and Pitx2+ SC-ZI pathways

(A) Sample micrographs showing the expression of ChR2-mCherry in the Cbln2+ SC neurons of Cbln2-IRES-Cre mice (left) and the optical fiber track above the ChR2-mCherry+ axons in the LPTN (right). **(B)** Schematic diagram showing the behavioral paradigm for the light-evoked freezing response in an arena. **(C)** Time courses of the locomotion speed of mice before, during and after light stimulation (10 Hz, 20 ms, 5 mW, 5 s) of the Cbln2+ SC-LPTN pathway expressing ChR2-mCherry (ChR2) or mCherry (Ctrl). **(D)** Quantitative analysis of the locomotion speed of mice before, during and after light stimulation of the Cbln2+ SC-LPTN pathway expressing ChR2-mCherry (ChR2) or mCherry (Ctrl). **(E)** Sample micrographs showing the expression of ChR2-mCherry in the Pitx2+ SC neurons of Pitx2-Cre mice (left) and the optical fiber track above the ChR2-mCherry+ axons in the ZI (right). **(F)** Schematic diagram showing the behavioral paradigm for prey capture paired with light stimulation of the Pitx2+ SC-ZI pathway. **(G)** Behavioral ethograms of predatory hunting in mice without (Laser OFF) and with (Laser ON) light stimulation of the Pitx2+ SC-ZI pathway. **(H-J)** Quantitative analyses of latency to attack (H), time to capture (I) and attack frequency (J) in mice without (OFF) and with (ON) light stimulation of the Pitx2+ SC-ZI pathway. **(K)** Schematic diagram showing a mouse encountering a cruising aerial predator or a terrestrial prey in the natural environment. **(L)** Yin-Yang circuit modules formed by Cbln2+ and Pitx2+ SC neurons and their downstream target areas. The Cbln2+ SC neurons in the “Yin” module detect the sensory features of cruising aerial predators and initiate freezing as a defensive response for the avoidance of predators through the Cbln2+ SC-LPTN pathway. The Pitx2+ SC neurons in the Yang module mediate tactile-triggered prey capture behavior through the Pitx2+ SC-ZI pathway. The data in (C, D, H-J) are presented as mean ± SEM (error bars). The statistical analyses in (D, H-J) were performed using Student’s t-test (n.s. $P>0.1$; * $P<0.05$; ** $P < 0.01$; ***$P<0.001$). For the P values, see Table S9. Scale bars are indicated in the graphs.

Figure S1 Quality of snRNA-seq metrics and the spatial distribution of neurons

(A) Number of genes (nGene) and number of unique molecular identifiers (nUMI) of the two snRNA-seq experiment replicates presented in violin plot. Replicate 1 (sample-1) is colored in yellow and replicate 2 (sample-2) is colored in blue. Each dot represents an individual cell.

(B) t-SNE plot of the two replicates of single-cell RNA-seq experiment. Replicate 1 (sample-1) is colored in yellow and replicate 2 (sample-2) is colored in blue. Each dot represents an individual cell.

(C) Heatmap of top50 differentially expressed genes (DEGs) of each major cell type shown in Figure 1A. The scale bar indicates relative gene expression level (purple, low; yellow, high).

(D) Spatial expression of the top DEGs of excitatory neuron subclusters and inhibitory neuron subclusters. Upper panel: gene expression levels projected onto the two-dimensional t-SNE and colored according to relative gene expression level (gray, low; red, high). Red dashed line, excitatory neuron subclusters; blue dashed line, inhibitory neuron subclusters. Lower panel: In situ hybridization staining of mouse superior colliculus for the identified excitatory neuron layer markers (from the Allen Brain Atlas).

Figure S2 Electrophysiological properties and the expression of DEGs between LPTN- and ZI- projecting SC neurons

(A) Schematic diagram showing current-clamp whole-cell recording from LPTN- or ZI-projecting SC neurons labeled with EGFP.

(B, C) Quantitative analyses of resting membrane potential (B) and firing threshold (C) of SC neurons that project to the LPTN (LPTN) and ZI (ZI).

(D) Example traces of action potential firing evoked by depolarizing currents injected into EGFP+ LPTN-projecting and ZI-projecting SC neurons.

(E) Quantitative analyses of spike number as a function of current intensity. Scale bar is indicated in the graph.

(F) Patch-seq strategy of LPTN-projecting neurons from OP and ZI-projecting neurons from InG in SC. A representative example was given to show how the fluorescence labeled cells were picked (bottom).

(G) Violin plots showing the quality control metrics of the scRNA-seq experiments by Patch-seq. Each dot represents an individual cell. Red represents ZI-projecting neurons from the InG layer in SC. Blue represents LPTN-projecting neurons from the OP layer in SC.

(H) In situ hybridization visualization (from Allen Brain Atlas) of genes presented in Figure 2 J.

(I) Examples of gene expression pattern and in situ hybridization visualization (from Allen Brain Atlas) of the DEGs presented in Figure 2I. The scale bar indicates relative gene expression level (blue, low; yellow, high).

(J) t-SNE plot visualizing the expression of differentially expressed genes between LPTN-projecting (upper panel) or ZI-projecting (lower panel) neurons by same layout as Figure 1A. The scale bar indicates the relative gene expression level. (gray, low; red, high). Red dash line: Op layer excitatory neuron subclusters.; blue dash line: InG layer excitatory neuron subclusters. Data in (B, C, E) are mean ± SEM. Statistical analyses in (B, C) were performed with Student t-test (n.s., P>0.1). Statistical analysis in (E) was

performed with One-Way ANOVA (n.s., P>0.1). For P values, see Table S9.

Figure S3 Generation of Cbln2-IRES-Cre mice to test the function of Cbln2+ and Pitx2+ SC neurons

(**A**) Heatmap showing the computed layer specificity score of ten DEGs of LPTN-projecting and ZI-projecting neurons.

(B) Schematic diagram of CRISPR/Cas9-mediated knock-in of a Cre coding cassette into downstream of Cbln2 gene of mice. The Cre expression was driven by IRES.

(C) Top, PCR amplification of Cre cassette knock-in at the endogenous Cbln2 gene locus. Arrows indicate PCR amplification of the genome joint with the left homologous arm (Up, 2713 bp) or the right homologous arm (Down, 1617 bp), and part of the Cre report cassette. The primers used for PCR amplification are indicated in (B) and shown in Table S6. PCR amplicons were cloned and sequenced for insertion analysis. Samples #2, #3, #6, #7 and #11 showed correct recombination. The insertion information was furthered confirmed by Sanger sequencing. M indicates marker DL2000 (Takara). Bottom, the chromatographs from the sequence files showed that CRISPR/Cas9-mediated precise insertion at the target locus.

(D) Example micrographs showing, in Cbln2-IRES-Cre mice, the Cbln2+ SC neurons labeled by EGFP were predominantly positive for vGlut2 mRNA (first row), while they were mostly negative for vGat mRNA (second row).

(E) Example coronal section of Cbln2-IRES-Cre mice showing expression of EGFP and TeNT in Cbln2+ SC neurons that were predominantly distributed in the SC Op layer.

(F) Behavioral ethograms of predatory hunting in example mice without (Ctrl) and with (TeNT) inactivation of Cbln2+ SC neurons.

(G-I) Quantitative analyses of latency to attack (G), time to capture (H), and attack frequency (I) of Cbln2-IRES-Cre mice without (Ctrl) and with (TeNT) inactivation of Cbln2+ SC neurons.

(J) Example micrographs showing, in Pitx2-Cre mice, the Pitx2+ SC neurons labeled by EGFP were predominantly positive for vGlut2 mRNA (first row), while they were mostly

negative for vGat mRNA (second row).

(K) Example coronal section of Pitx2-Cre mice showing expression of EGFP and TeNT in Pitx2+ neurons that were predominantly distributed in the SC intermediate layers (In).

(L) Time courses of locomotion speed of Pitx2-Cre mice without (Ctrl) and without (TeNT) inactivation of Pitx2+ SC neurons before, during and after the sweep of overhead moving visual target.

(M-O) Quantitative analyses of locomotion speed of Pitx2-Cre mice without (Ctrl) and with (TeNT) inactivation of Pitx2+ SC neurons before (M), during (N), and after (O) the sweep of overhead moving visual target.

Data in (G-I, M-O) are mean ± SEM. Statistical analyses in (G-I, M-O) were performed with Student t-test (n.s., P>0.1). For P values, see Table S9. Scale bars are indicated in the graph.

Figure S4 Sensory response properties of Cbln2+ and Pitx2+ SC neurons

(A) Distribution of receptive field centers (red spots) of recorded Cbln2+ SC neurons in five Cbln2-IRES-Cre mice in the meridian plot of the mouse retina on the tangent screen. The coordinate origin of the meridian plot was the visual axis. Concentric circles were spaced by 15º visual angles. Note the receptive fields of Cbln2+ SC neurons were localized within the dorsal quadrant, consistent with their role in detecting aerial predator.

(B) Normalized GCaMP fluorescence changes (ΔF/F) of Cbln2+ SC neurons in response to air-puffs directed toward contralateral or ipsilateral vibrissal area with different strengths (10, 20, 30 p.s.i.).

(C) Normalized GCaMP fluorescence changes (ΔF/F) of Pitx2+ SC neurons in response to a black circle (5°) moving (32°/s) in different directions (T-to-N, N-to-T, V-to-D, D-to-V). N, D, T and V represent nasal, dorsal, temporal and ventral, respectively.

(D) Normalized GCaMP fluorescence changes (ΔF/F) of Pitx2+ SC neurons in response to a black circle (5°) moving (T-to-N) with different velocity (32°/s and 128°/s).

(E) Normalized GCaMP fluorescence changes (ΔF/F) of Pitx2+ SC neurons in response to a moving black circle with different diameters (5° and 25°) (T-to-N, 32°/s).

Figure S5 RV tracing of Cbln2+ and Pitx2+ SC neurons

(A, B) Example micrographs showing the expression of EGFP (green) and DsRed (red) in the Cbln2+ and Pitx2+ neurons in the SC of Cbln2-IRES-Cre (A) and Pitx2-Cre mice (B), respectively. Note the dually-labeled cells indicate starter cells.

(C-F) Example micrographs showing DsRed+ cells in different brain regions, including contralateral spinal trigeminal nucleus interpolar part (Sp5I) and the PCRt (C), the ipsilateral zona incerta (ZI) (D), the substantia nigra reticular part (SNr) (E), and the ipsilateral M1/M2 & Cg1/2 (F) of Cbln2-IRES-Cre and Pitx2-Cre mice.

Figure S6 Efferent projections of Cbln2+ and Pitx2+ SC neurons

(A) Schematic diagram showing the strategy to map the efferent projections of Cbln2+ and Pitx2+ SC neurons.

(B) Example coronal sections of Cbln2-IRES-Cre and Pitx2-Cre mice showing the distribution of infected neurons in the SC.

(C-F) Example micrographs showing EGFP+ axons of Cbln2+ and Pitx2+ SC neurons in the target brain regions at the level of thalamus (C), midbrain (D), pons (E), and medulla (F). Abbreviations: LPTN, lateral posterior thalamic nucleus; PF, parafascicular nucleus; ZI, zona incerta; Pn, pontine nucleus; LPB, lateral parabrachial nucleus; IO, inferior olive; PCRt, parvicellular reticular nucleus; LDTg, laterodorsal tegmental nucleus; IRt, intermediate reticular nucleus; PAG, periaqueductal gray; ECIC, external cortex of the inferior colliculus; Tz, nucleus of the trapezoid body. Scale bars are labeled in the graphs.

Figure S7 Activation of Cbln2+ SC-LPTN pathway and Pitx2+ SC-ZI pathway

(A) Schematic diagram showing whole-cell recording from ChR2-mCherry+ SC neurons in the acute brain slice.

(B, C) Example traces of phase-locked spiking activity evoked by light-pulse train (1 ms, 5 mW) in 10 Hz (top) or 20 Hz (bottom) from Cbln2+ SC neurons (B) or Pitx2+ SC neurons (C) that expressed ChR2-mCherry in acute brain slices.

(D) Behavioral ethogram of predatory hunting in mice without (Laser OFF) and with (Laser ON) light stimulation of Cbln2+ SC-LPTN pathway.

(E) Quantitative analyses of latency to attack (left), time to capture (middle), and attack frequency (right) in mice without (Laser OFF) and with (Laser ON) light stimulation of Cbln2+ SC-LPTN pathway.

(F) Time courses of locomotion speed before, during and after light stimulation of Pitx2+ SC-ZI pathway that expressed mCherry (Ctrl) or ChR2-mCherry (ChR2).

(G) Quantitative analyses of locomotion speed before, during and after light stimulation of Pitx2+ SC-ZI pathway that expressed mCherry (Ctrl) or ChR2-mCherry (ChR2).

Data in (E-G) are mean ± SEM. Statistical analyses in (E, G) were performed with Student t-test (n.s., P>0.1). For P values, see Table S9.

Supplementary Tables

Table S1. Sample information for high-throughput snRNA-seq of nucleus from superior colliculus (SC) and top50 differentially expressed genes among 9 major cell types in SC, related to Figure 1A.

Table S2. Differentially expressed genes among 9 excitatory neuron subtypes and 10 inhibitory neuron subtypes, related to Figure 1C and 1D.

Table S3. Sample information for Patch-seq of neurons from superior colliculus (SC), related to Figure 2H.

Table S4. Differentially expressed genes between ZI- and LPTN-projecting neurons in SC, related to Figure 2I.

Table S5. Differentially expressed genes between excitatory neuron subtype Ex-3 and Ex-6, and between Ex-1 and Ex-4, related to Figure 2L, 2M respectively.

Table S6. Information of mouse lines and reagents.

Table S7. Summary of all experimental designs.

Table S8. Summary of cell-counting strategies.

Table S9. Summary of statistical analyses.

Supplementary Movies

Movie S1.3D reconstruction of layer-specific neuron projection patterns from SC to downstream brain regions by in vivo sparse-labeling strategy and M-CRITIC, related to Figure 2B and 2C.

Movie S2. An example movie showing that synaptic inactivation of Cbln2+ SC neurons by TeNT impaired visually-evoked freezing responses. Related to Figure 3D.

Movie S3. An example movie showing that synaptic inactivation of Pitx2+ SC neurons by TeNT impaired prey capture behavior in the arena. Related to Figure 3K.

Movie S4. An example movie showing that light stimulation of ChR2-mCherry+ axon terminals of Cbln2+ SC neurons in the LPTN induced freezing response in mice. Related to Figure 7B and 7C.

Movie S5 An example movie showing light stimulation of ChR2-mCherry+ axon terminals of Pitx2+ SC neurons in the ZI promoted predatory hunting behavior in mice, related to Figure 7F and 7G.

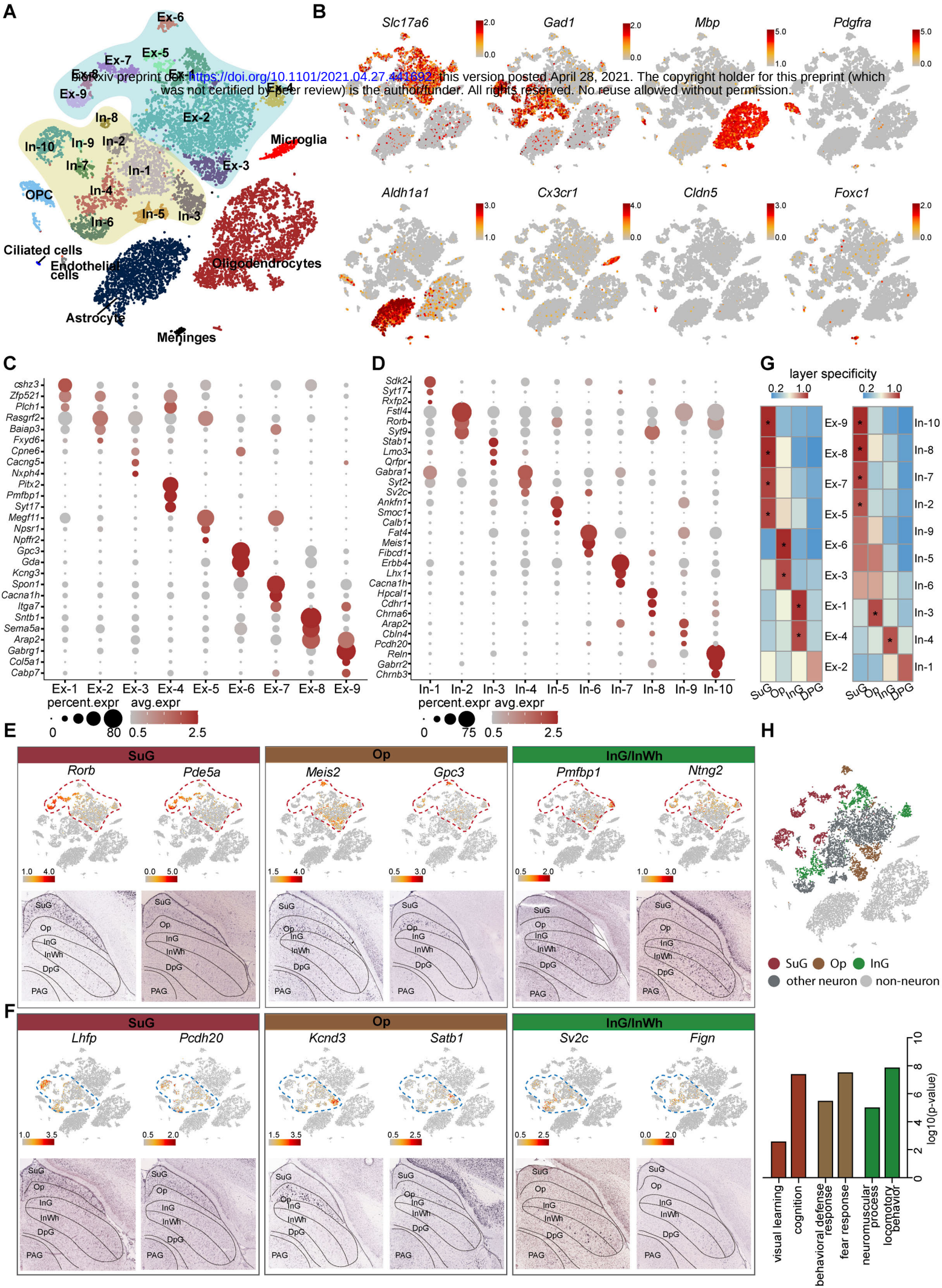

Figure 1 A census of SC cell types using snRNA-seq

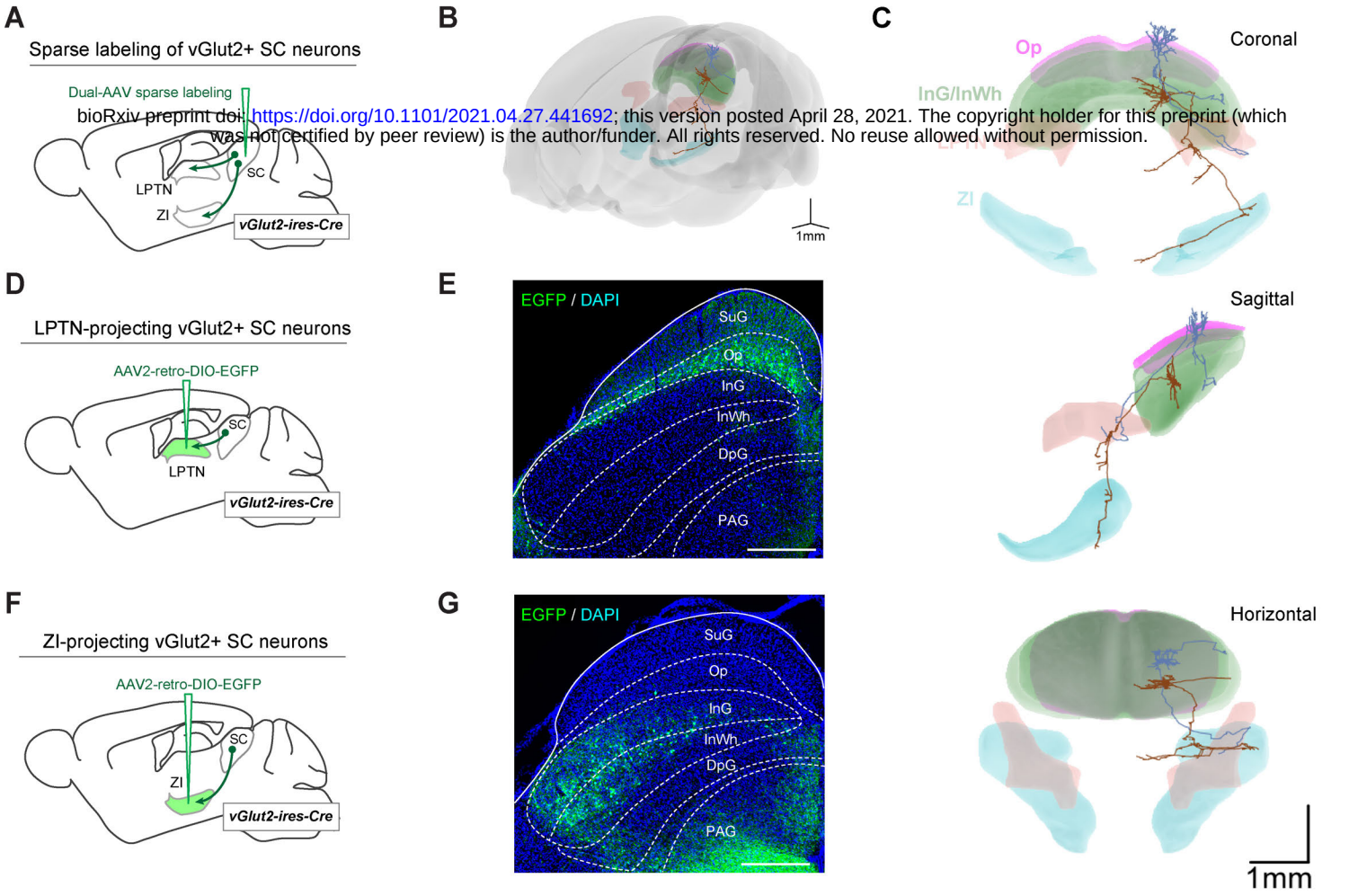

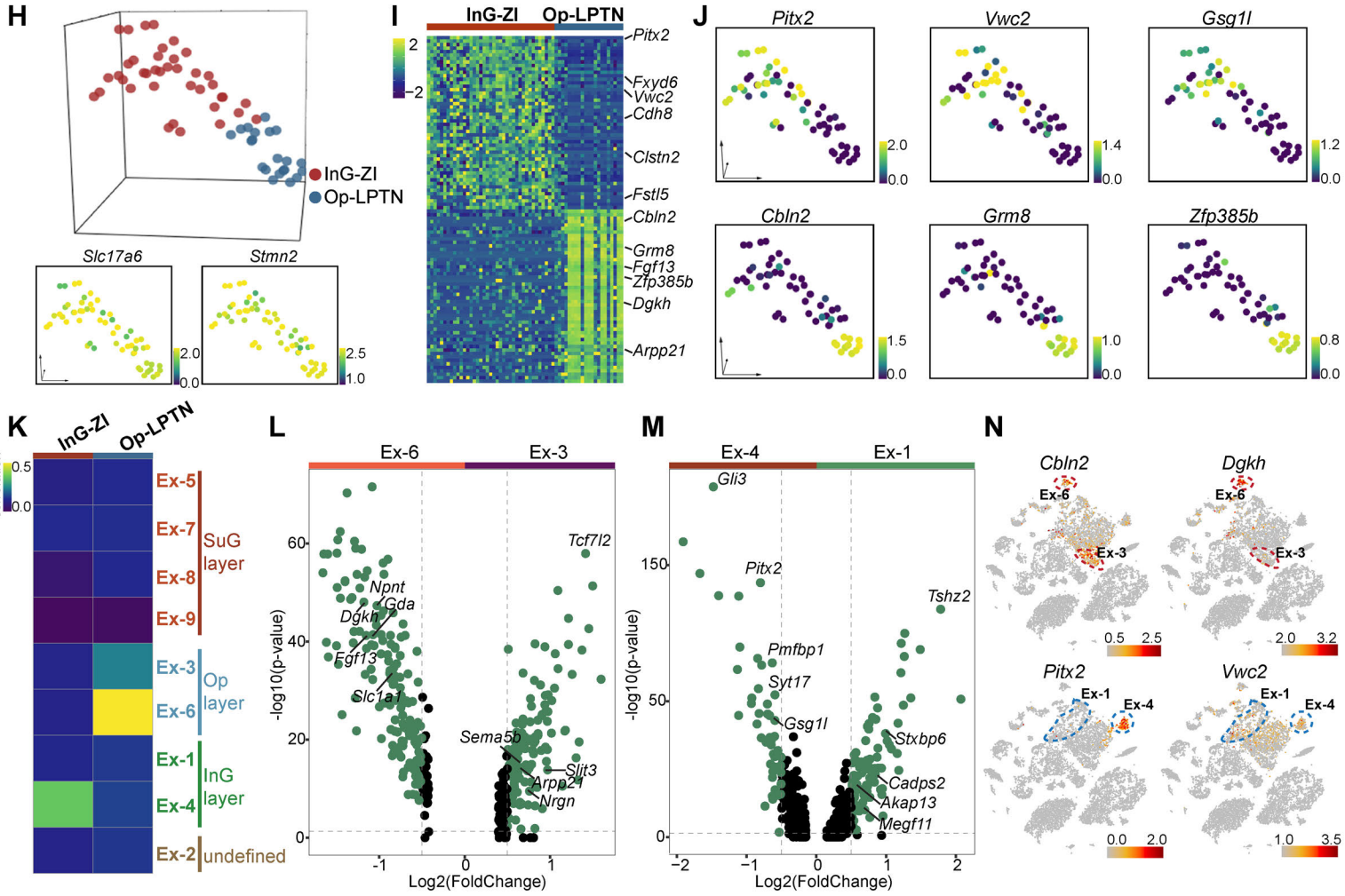

Figure 2 Circuit-specific single-cell transcriptomic analysis by Patch-seq

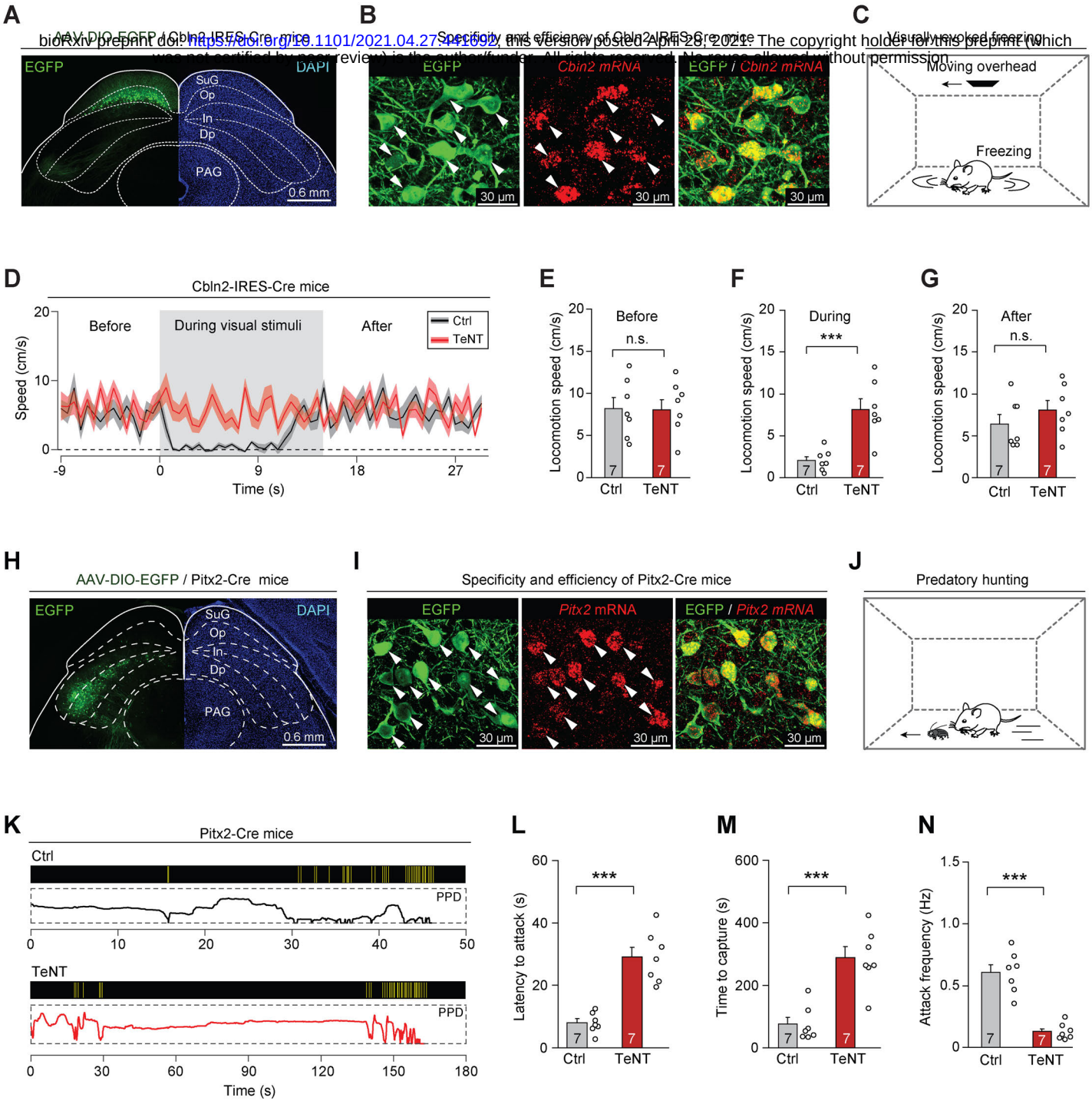

Figure 3 Inactivation of Cbln2+ and Pitx2+ SC neurons

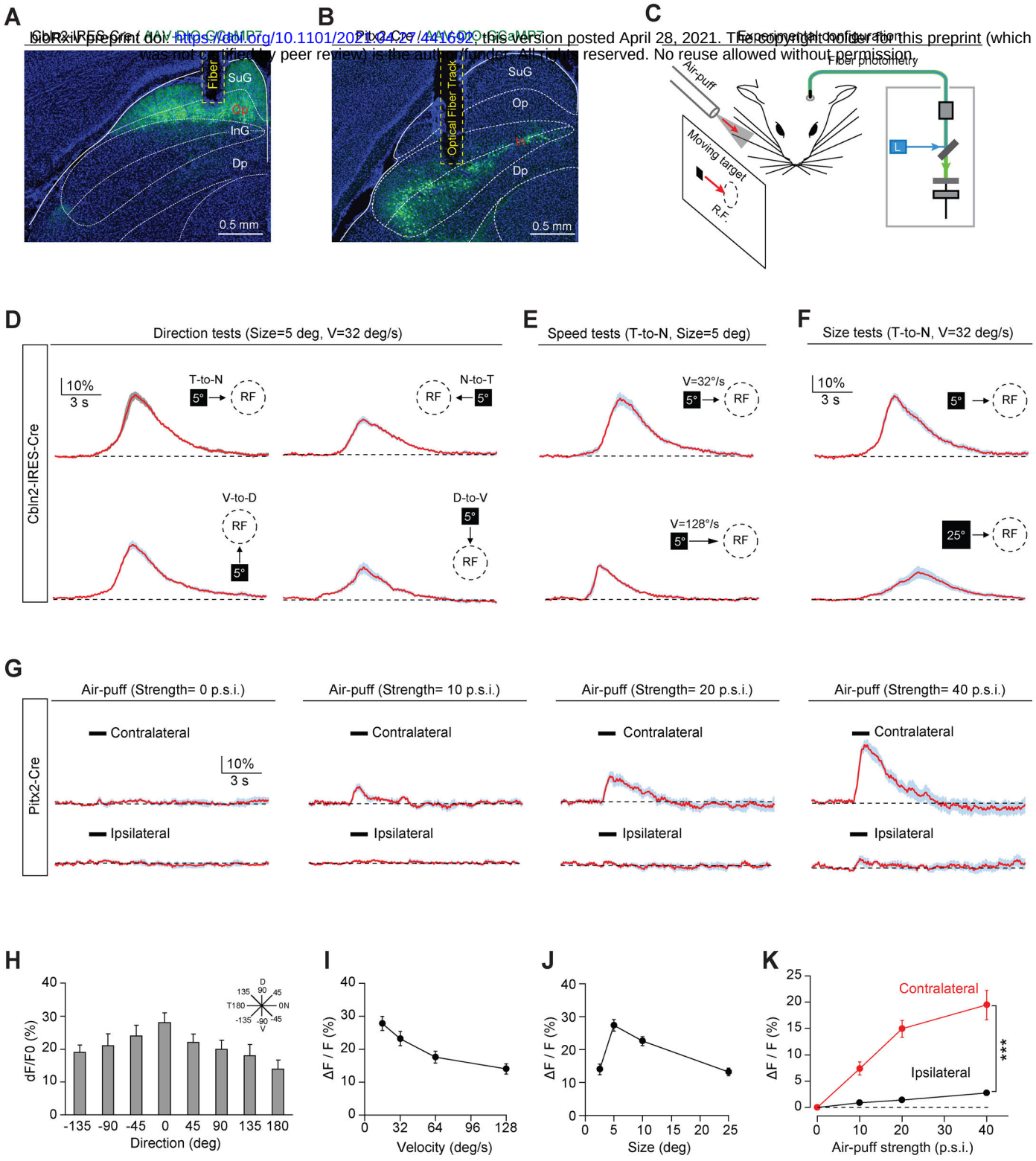

Figure 4 Sensory responses

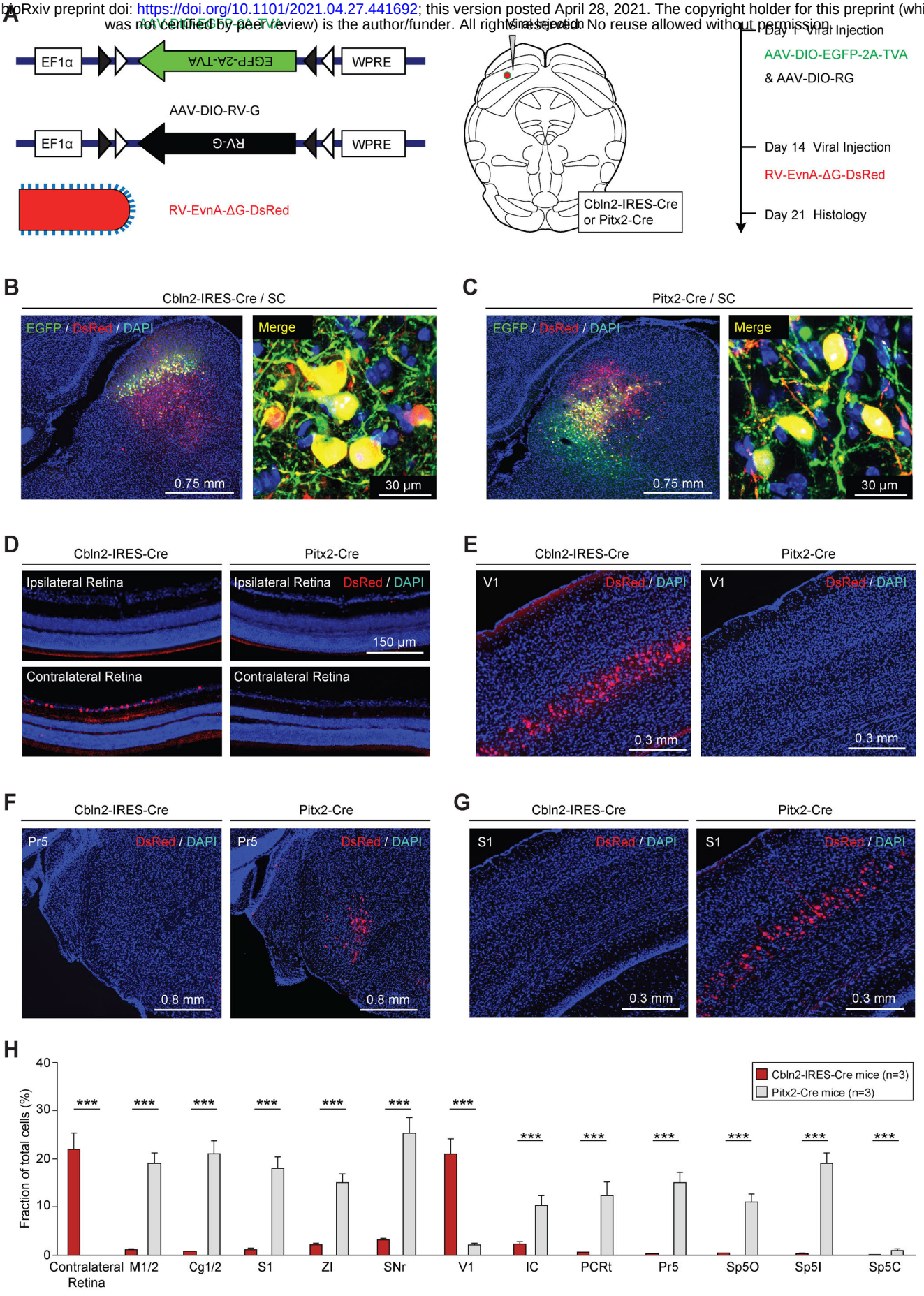

Figure 5 RV tracing

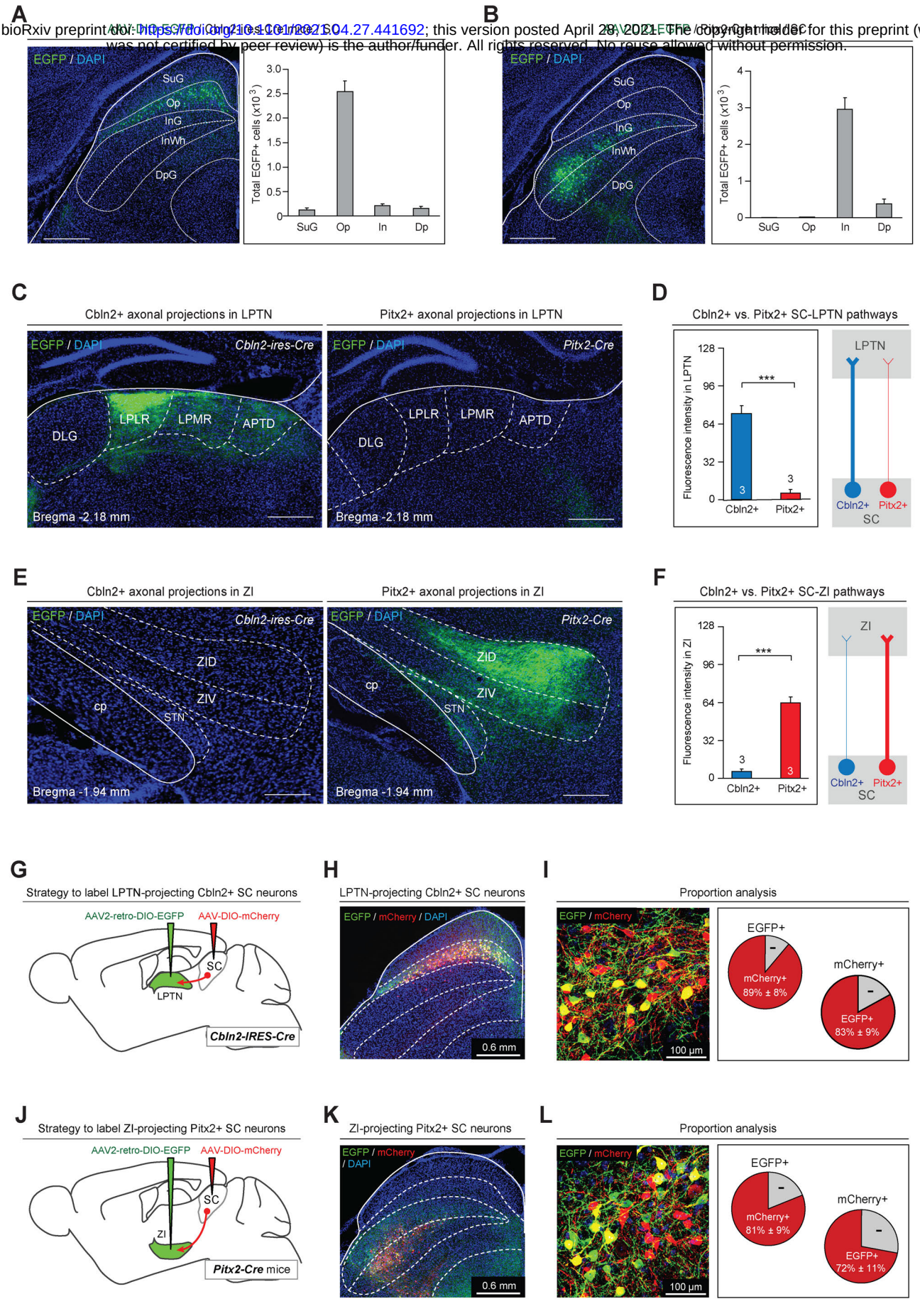

Figure 6 Projection of Cbln2+ and Pitx2+ neurons

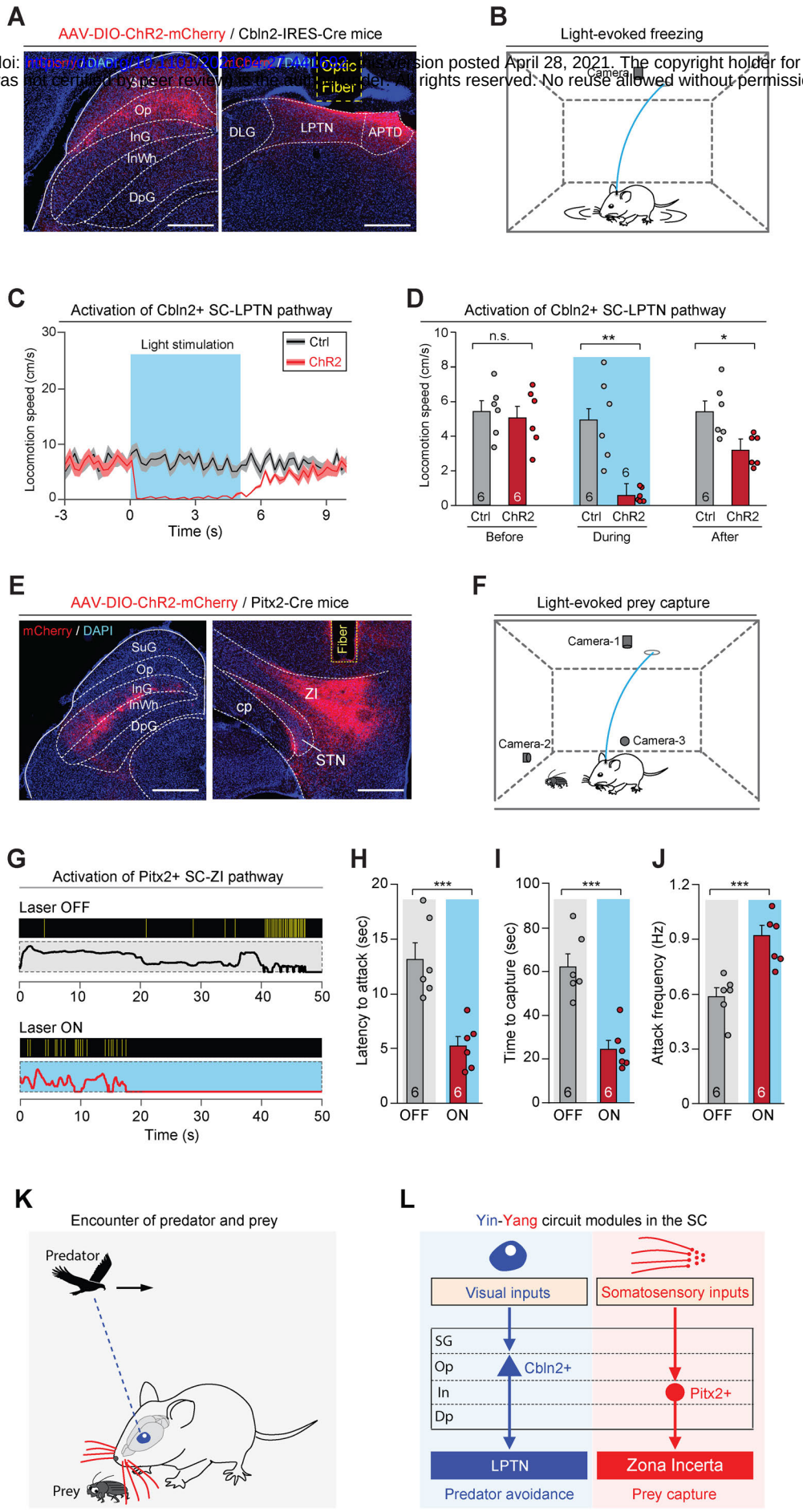

Figure 7 Activation of individual pathways

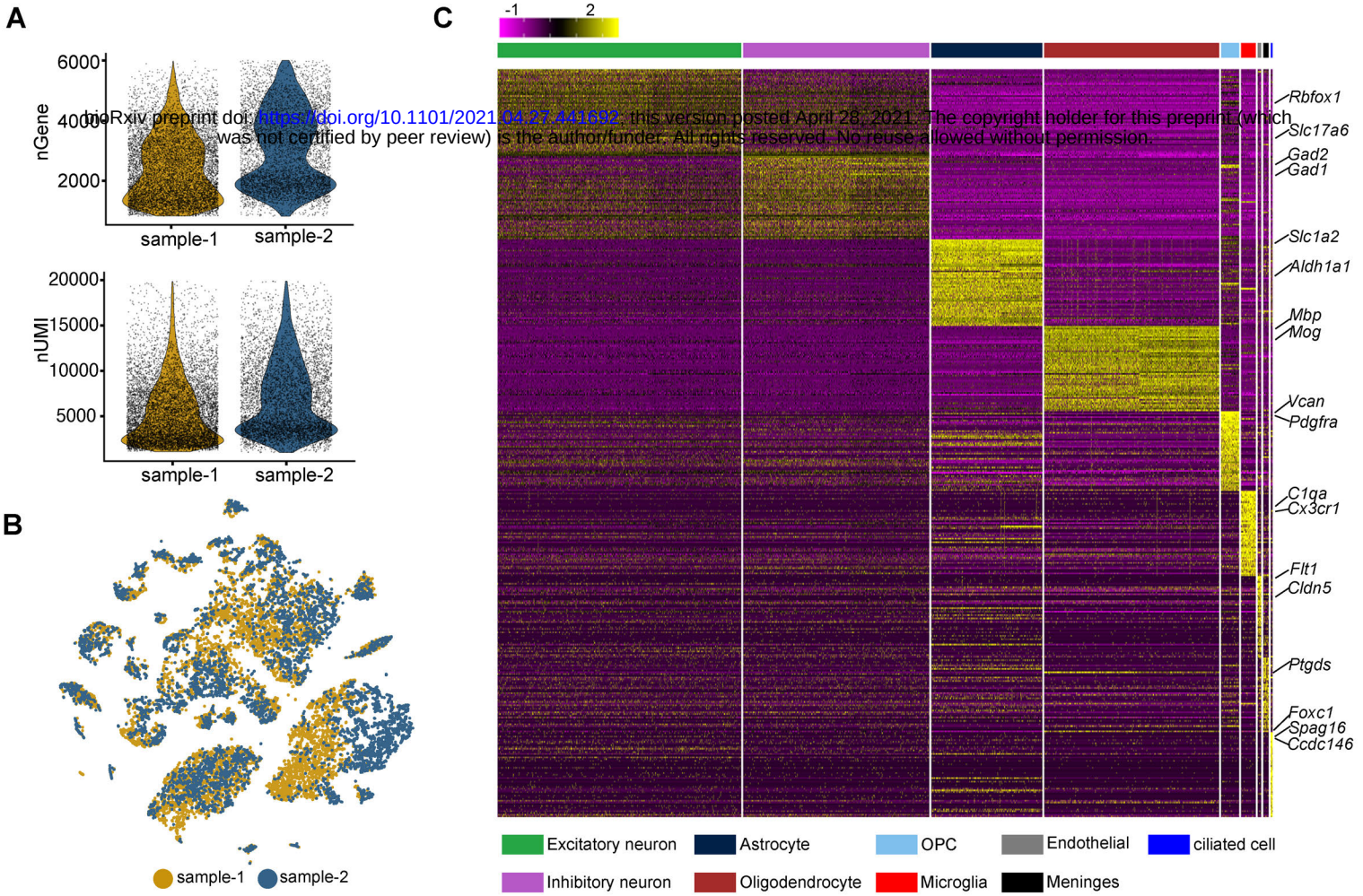

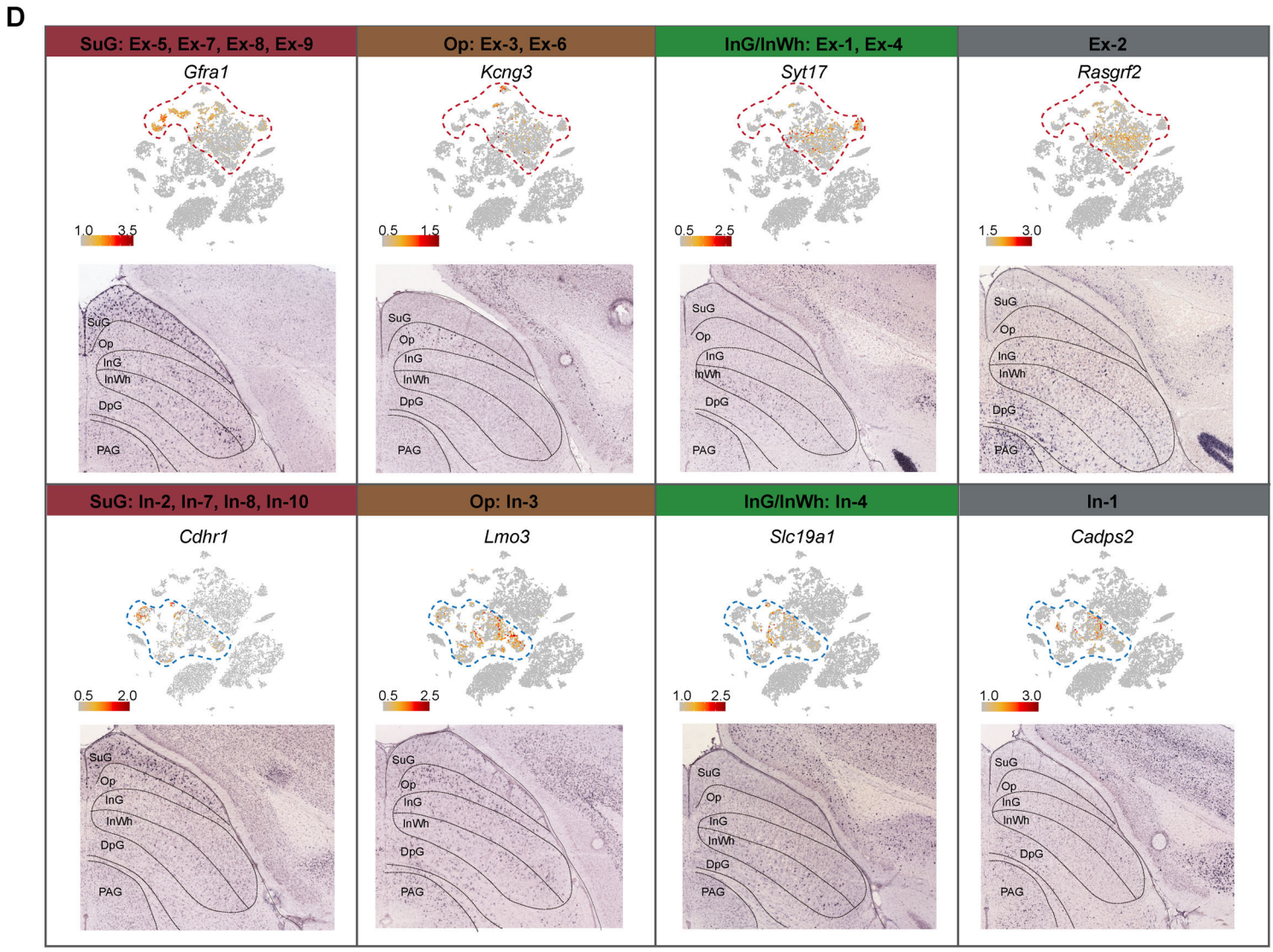

Figure S1 High-throughput snRNA-seq of human SC

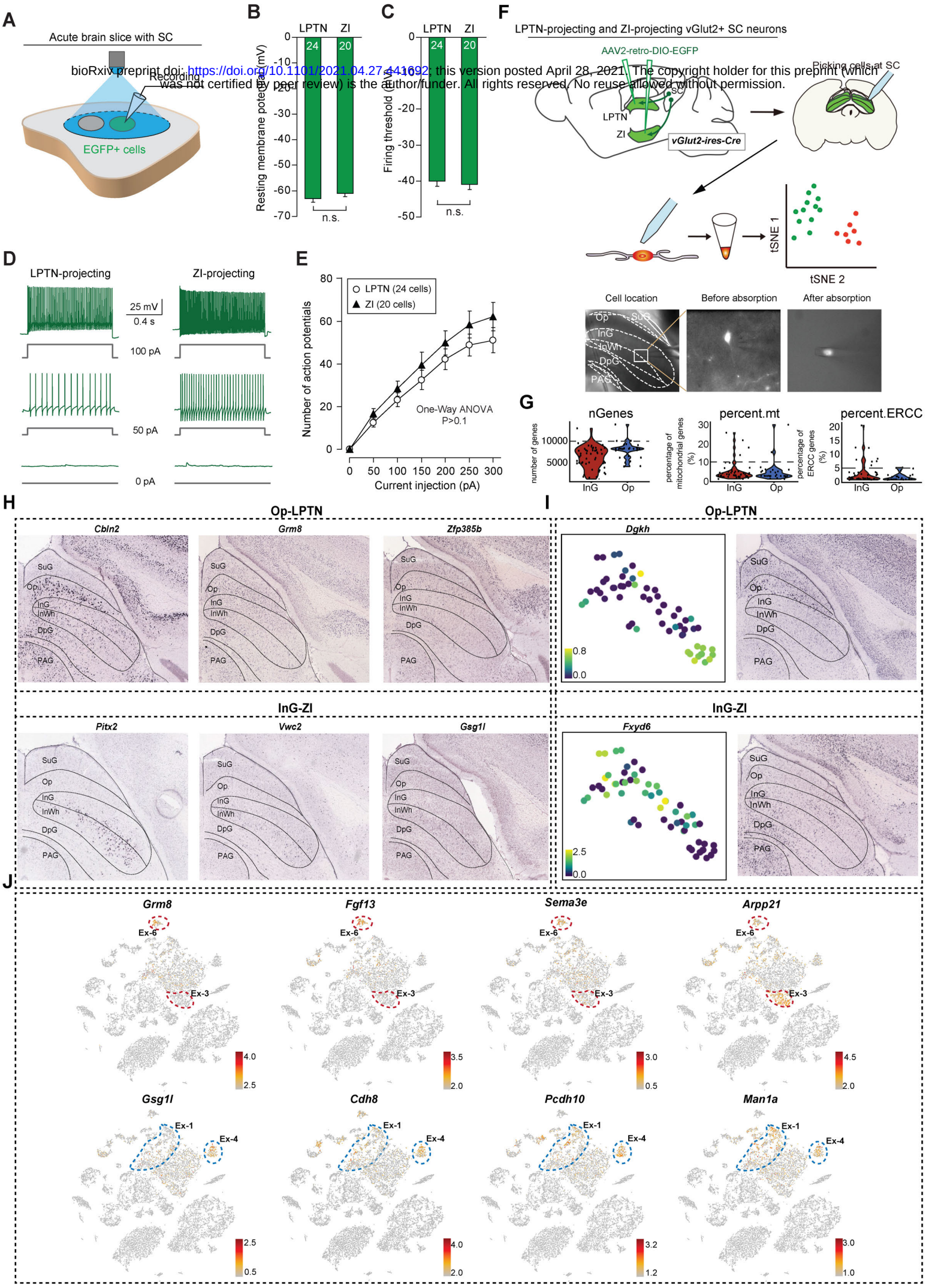

Figure S2 Patch-seq of Op-LPTN and InG-ZI neurons

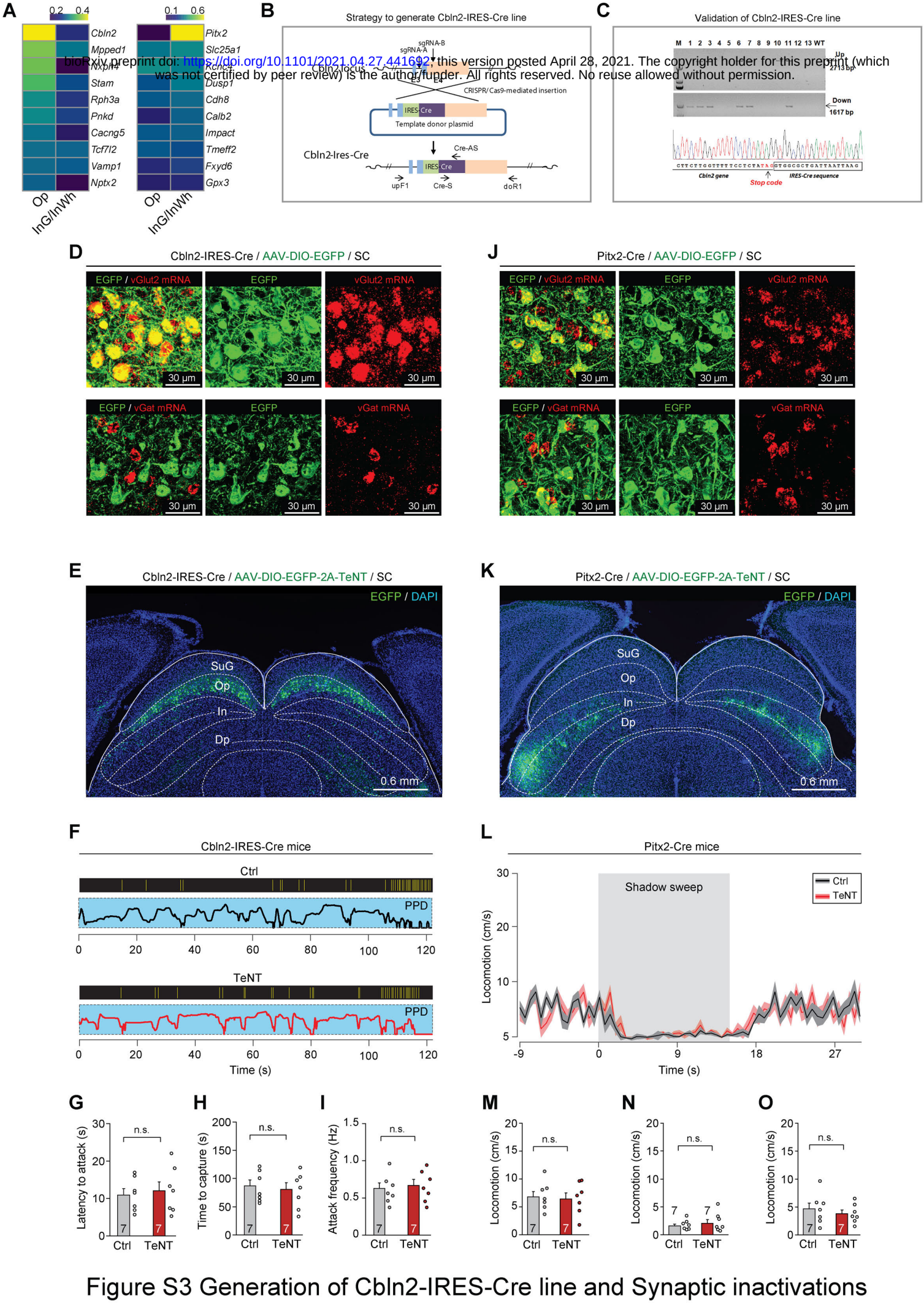

Figure S3 Generation of Cbln2-IRES-Cre line and Synaptic inactivations

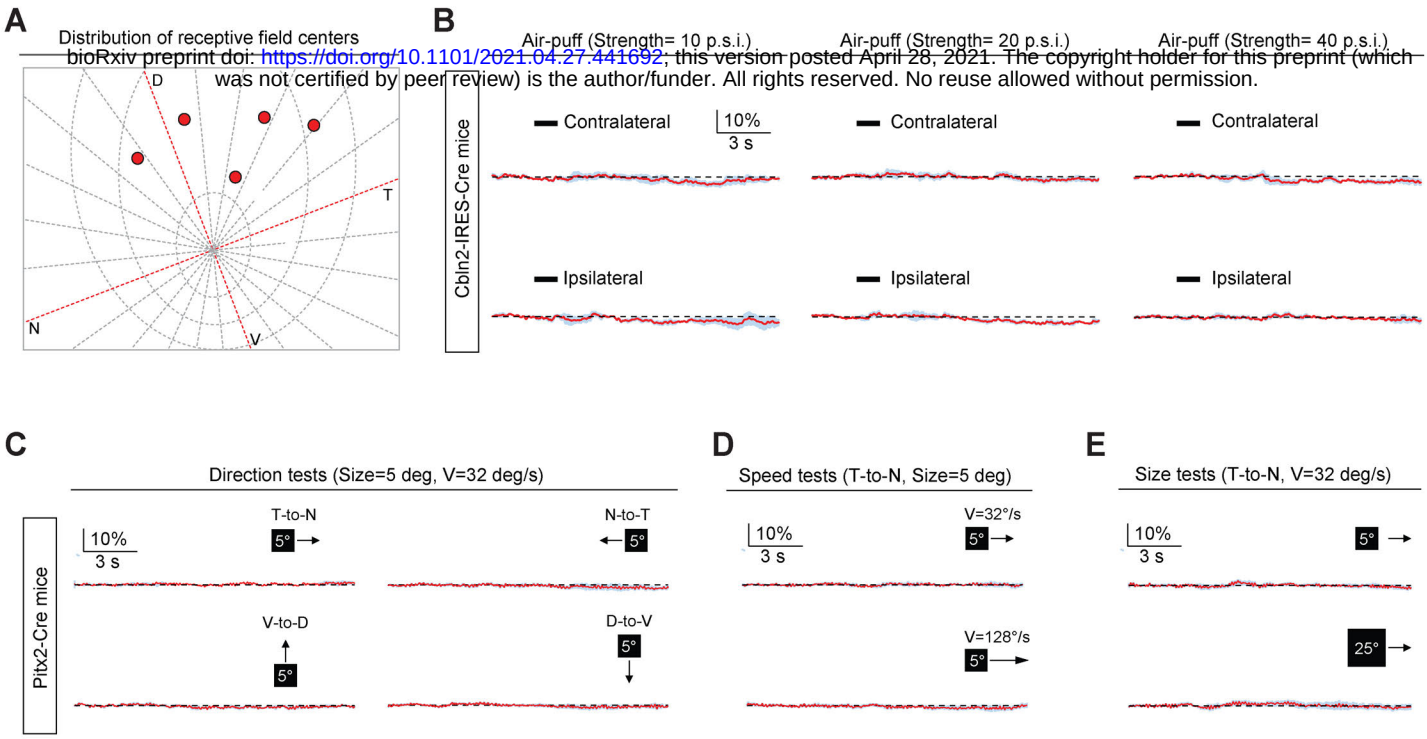

Figure S4 Fiber photometry

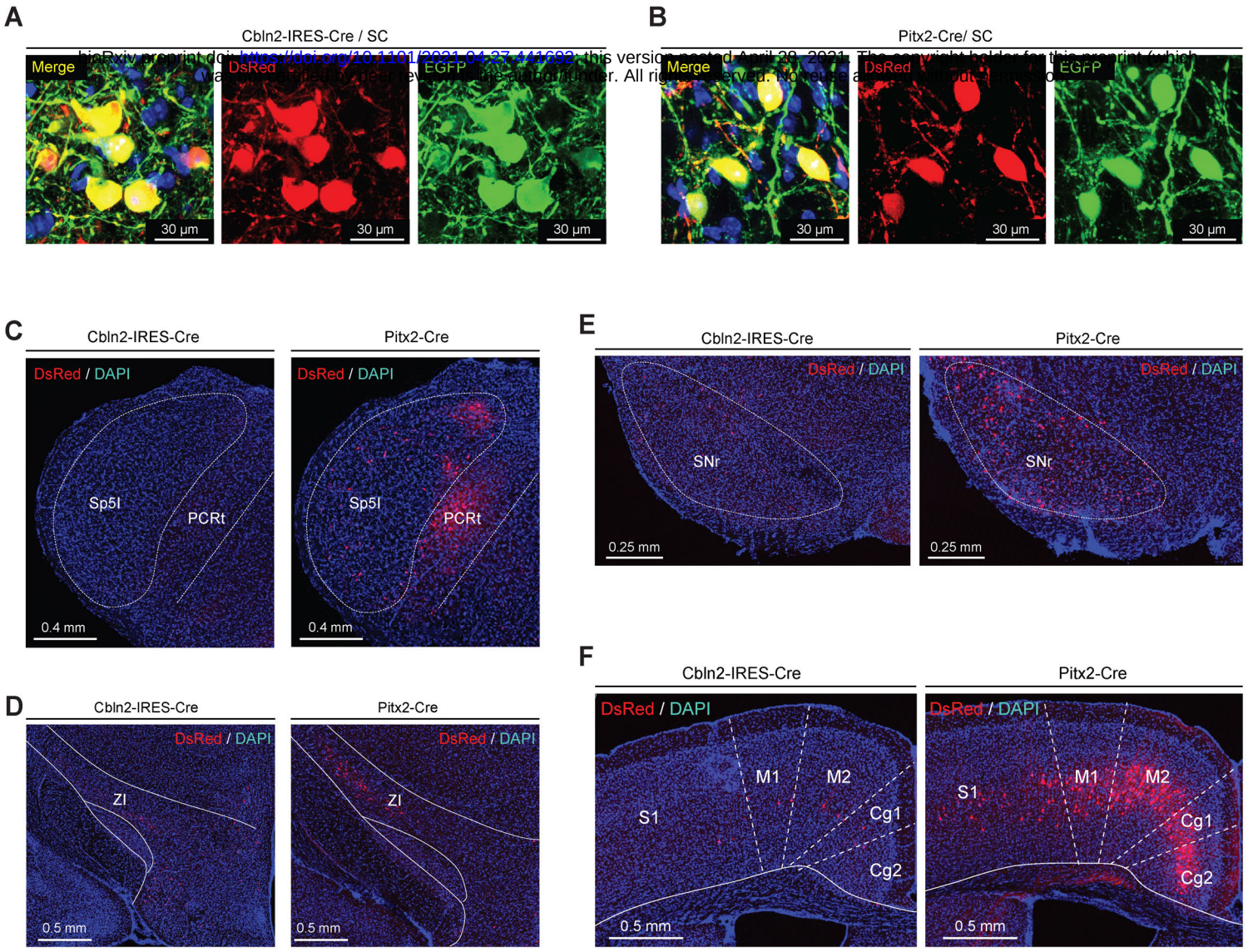

Figure S5 RV tracing

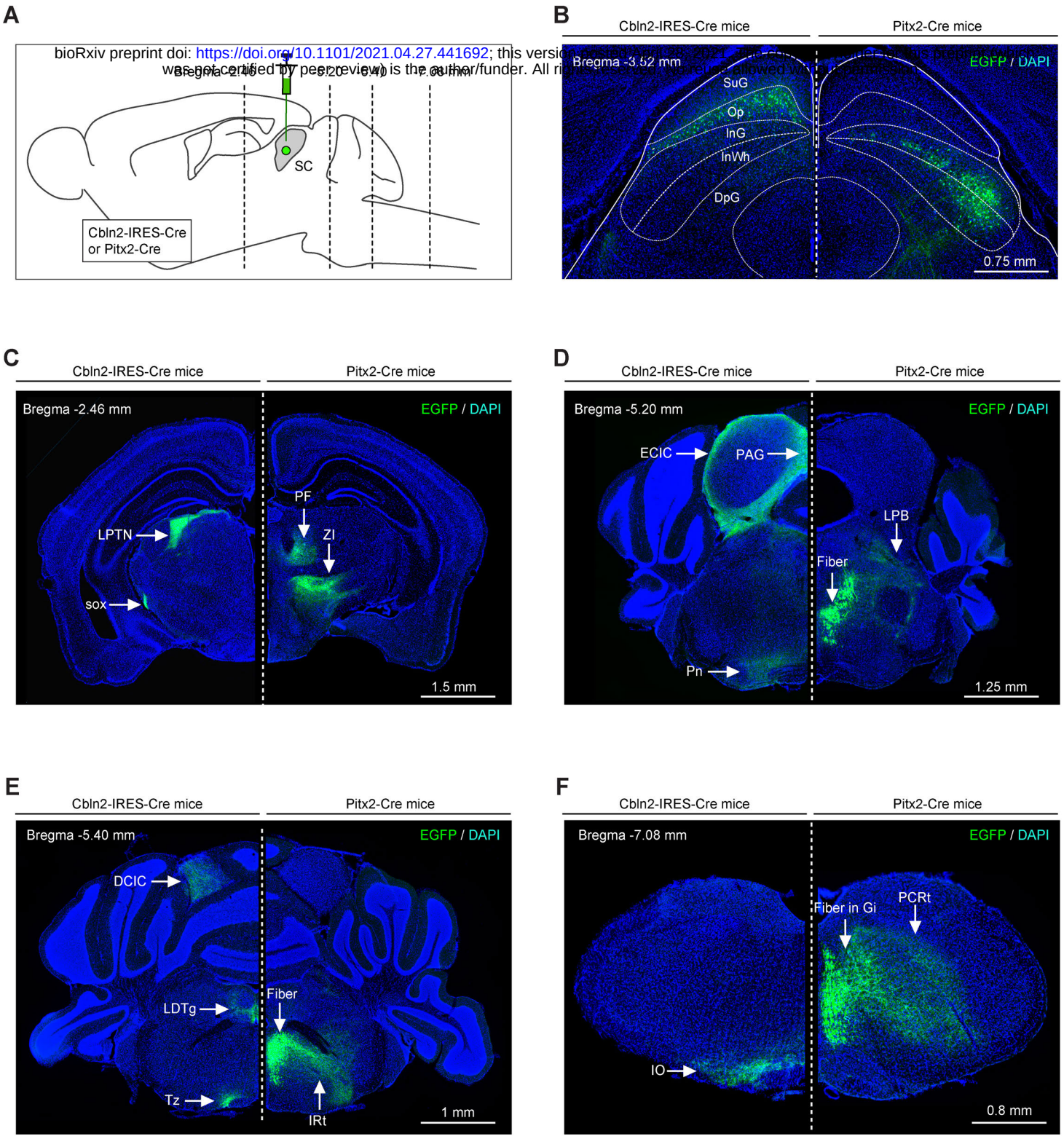

Figure S6 Divergent projections

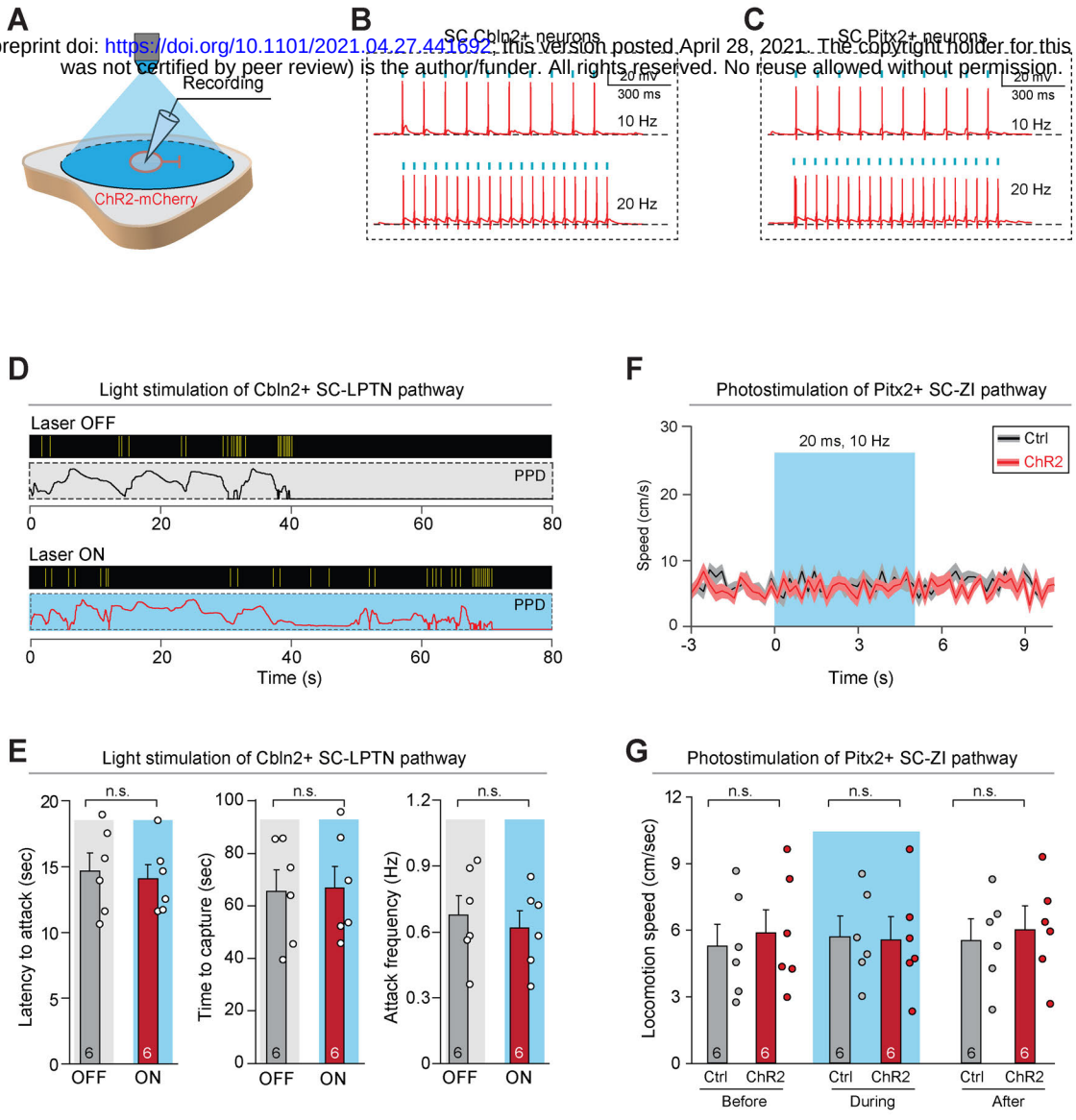

Figure S7 Pathway Activation